Rhythms and Background (RnB): The Spectroscopy of Sleep Recordings

J. Dubé [1,2], M. Foti [3], S. Jaffard [4], V. Latreille [5], B. Frauscher [6], J. Carrier [1,2], J.M. Lina [2,3,7]

1. Department of Psychology, Université de Montréal, Montreal, Qc, Canada
2. Center for Advanced Research in Sleep Medicine, Hop. Sacré-Cœur de Montréal, Montreal, Qc, Canada
3. Electrical Eng. Dep., École de Technologie Supérieure, Montreal, Qc, Canada
4. LAMA, Univ. Paris-Est-Créteil, France
5. Department of Neurology and Neurosurgery, Montreal Neurological Institute Hospital, McGill University. Montreal, Canada.
6. Department of Neurology, Analytical Neurophysiology Lab., Duke University, North Carolina, United States.
7. Centre de Recherches Mathématiques, Université de Montréal, Montreal, Canada

Abstract (150 words)

Non-rapid eye movement (NREM) sleep is characterized by multiple coupled rhythms involved in memory consolidation, alongside an arrhythmic 1/f scale-free background also hypothesized to contribute to NREM sleep functions. Spectral parametrization methods have been recently introduced to describe the properties of rhythmic and arrhythmic processes in the spectral domain. However, these approaches fall short disentangling rhythms from arrhythmicity regarding the time series. This is crucial as arrhythmicity can impact the morphology of individual oscillations, therefore affecting their frequency, amplitude, waveform, and their cross-frequency coupling estimated transiently. We introduce 'Rhythms & Background' (RnB), an innovative wavelet-based methodology that compensates for arrhythmicity within the time domain. We validate RnB against spectral methods and demonstrate its enhanced capability to characterize the hallmark features of NREM sleep rhythms. Furthermore, RnB reveal the rhythmic time series, highlighting key NREM sleep rhythms with improved sensitivity to their phase-amplitude coupling.

Introduction (495)

Brain rhythms from bioelectric activity reflect synchronization of neuronal assemblies and are often inventoried using the Fourier analysis of electrophysiological brain recordings[1]. Non-rapid eye movement (NREM) sleep is characterized by cardinal rhythms critically involved in overnight information processing such as sleep slow waves (SSW, 0.5-4 Hz), theta bursts (6-10 Hz), sleep spindles (8-16 Hz), and sharp-wave ripples (100-200 Hz). These rhythms are organized in complex wave sequences, with sporadic amplitude-phase coupling across frequencies, which occur locally and between remote brain regions[2,3]. For instance, sleep spindles usually occur after SSWs' down states, within the transition period towards their upstate. The loss of specificity of this phase coupling in aging may contribute to impaired memory consolidation[4].

Alongside brain rhythms, new hypotheses suggest that arrhythmic brain activity plays complementary roles in NREM sleep functions[5]. Arrhythmic activity recruits a broad range of frequencies and is usually expressed as $1/f^{\beta}$ decay in the power spectral density [6]. This "scale-free" process, or arrhythmic component, is usually estimated using the spectral slope (β) expressed in the log-log power spectrum. The steepness of β has been related to the excitation-inhibition balance, supporting the notion that it may contribute to NREM-dependent plasticity processes[5,7]. Moreover, β differs among age groups, has been associated with cognitive impairment, and dynamically changes across sleep stages[8–11]. Importantly, arrhythmic differences in β alter the spectral peaks' characteristics (width, height, central frequency) are typically attributed to brain rhythms. Spectral parametrization methods, such as *Fitting-Oscillations-One-and-Over-F (FOOOF),* have thus been recently introduced to robustly assess rhythmic (peaks) and arrhythmic (β) components from the Fourier power spectrum[12,13].

Arrhythmicity is also expressed at the signal level as a ubiquitous 'desynchronized background' activity that nonlinearly interferes with transient oscillatory events[5,14]. This coexistence introduces noise in time-domain analyses, which decreases the robustness of phase and amplitude estimates and influences the detection of genuine rhythmic oscillations[14,15]. Currently, no method allows to correct for the impact of arrhythmicity at the time series level. The present work fills this important gap. Furthermore, we propose a data-driven approach to perform an inventory of NREM rhythmic events. Although blind source separation techniques could provide this inventory[16], such approaches will take advantage of the significant attenuation of the arrhythmic background obtained in the present work.

'Rhythms & Background' (RnB) is a wavelet-based algorithm designed to account for the arrhythmic background in NREM sleep's electrophysiological time series. RnB leverages

a reliable wavelet-based scale-free estimation alongside signal denoising to whiten $1/f$ activity during NREM sleep time series. This allows the extraction of a 'rhythmic time series' that can be further analyzed. We assessed its robustness and accuracy against established spectral methods in a simulation framework. We used RnB rhythmic time series to perform an inventory of NREM sleep rhythms and to investigate how intracranially recorded rhythmic SSWs harmonize other rhythms during NREM sleep. By extracting the rhythmic component as a new signal, this method opens new opportunities for time domain and time-scale (or time-frequency) analyses to improve our comprehension of rhythmic processes during sleep.

Results (2436)

RnB: The 'spectral paradigm' (292)

Spectral approaches perform an estimation of rhythms and background in the Fourier domain. Without loss of generality, we considered the following multiplicative model of the power spectral density (PSD; see *Methods 1.1* for details),

$$\Gamma(f) = P(f)\, e^{R(f)} \tag{1}$$

where $\Gamma(f)$ refers to the PSD of a time series, $P(f) = c/f^{\beta}$ accounts for arrhythmicity (as a constant and a slope), and $R(f)$ represents rhythms.

From this formalism, we first defined 'spectral-RnB' which estimates the rhythmic and arrhythmic components in the Fourier domain. Its usage is demonstrated on simulated time series (epochs), that combined scale-free (arrhythmic; Fig. 1, A1) backgrounds with oscillatory (rhythmic) activity from a neural mass model (Fig. 1, A2). For each epoch (indexed with 'i'), the arrhythmic factor $Q_i(f) \approx f^{-\beta_i}$ is reliably estimated from multiple rescaling transforms (see Methods section; Fig. 1, B1, B2). This allows estimating a scaling exponent β^* for each epoch, with or without a concurrent oscillation (Fig.1, D1, D2). This exponent is related to the Hurst exponent ($H = (\beta - 1)/2$) that describes the long-term memory of the time series[17]. $\beta > 2$ corresponds to a scale-free process with positive correlations (persistency), whereas $\beta < 2$ describes a process with an 'anti-persistent' memory and temporal anti-correlations. The whitened spectral content is estimated on an epoch-per-epoch basis (unshown) and the rhythmic factor $e^{R^*(f)}$ is estimated from the average of this residual spectra across all epochs,

$$e^{R^*(f)} = \langle Q_i(f)^{-1}\, \Gamma_i(f) \rangle \tag{2}$$

which reliably estimates the spectral signature of the simulated oscillation (Fig.1, E1, E2).

Contrasting with parametric methods such as FOOOF, which requires specifying the number of expected spectral peaks and the arrhythmic slope shape, spectral-*RnB* is non-parametric and data-driven[12.] Spectral-*RnB* produce a rhythmic and arrhythmic estimation for each epoch (Fig. 1B1 and B2). These characteristics will be carried over in the wavelet development of *RnB* in the upcoming section.

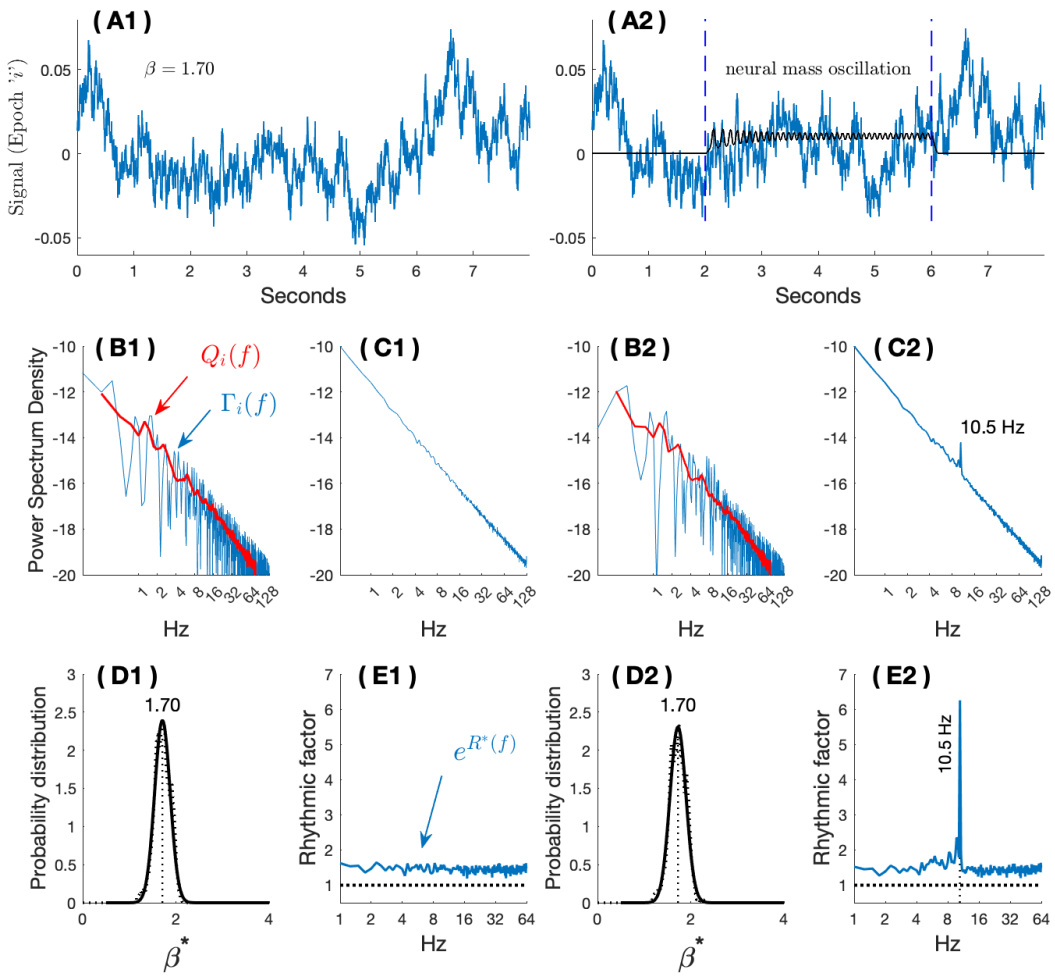

Fig.1. **Spectral$-$*RnB* estimation of arrhythmic background and rhythms. A1, A2,** Examples of two simulated time series, **A1** showing pure background arrhythmic activity (β =1.70; arrhythmic background). **A2** shows a mixture of the same arrhythmic activity as in **A1,** with the addition of a four second alpha oscillation (10.5 Hz). **B1, B2,** Fourier power spectra of **A1** and **A2**, respectively. The estimated arrhythmic spectrum $Q_i(f)$, as described above, is shown in red. **C1, C2**. Averaged standard power spectra over 250 simulations for each type of simulation as shown in B1 and B2. Even though the added oscillation in the signal (A2) is unnoticeable in the individual Fourier spectrum (B2), its signature is apparent in the averaged standard spectrum (C2). **D1, D2.** Probability density of estimated

scale-free exponents obtained from $Q_i(f)$ by Spectral-*RnB* in the two sets of 250 simulations, without **(D1)** and with **(D2)** the alpha 10.5 Hz oscillation. **E1, E2**, Rhythmic output by Spectral-*RnB*, that is the residual 'rhythmic factor' $\exp(R^*(f))$ controlled for the presence of arrhythmic background for the two sets of simulations, respectively without **(E1)** and with **(E2)** the alpha 10.5 Hz oscillation.

The 'wavelet-RnB paradigm' (392)

We considered a wavelet expansion of the previous model to resolve the entanglement between rhythms and arrhythmicity at the signal level. This approach produces a "rhythmic time series" that preserves the oscillatory content of the signal. Our algorithm is based upon this approach.

Wavelet-RnB denoises the signal from the arrhythmic background by performing the synthesis of the *rhythmic signal* $s_R(t)$ in the wavelet basis $\left\{\psi_{jk}^{(\alpha)}\right\}$ from the wavelet coefficients ${w_{jk}}^*$ obtained through the processing of the original signal $s(t)$ (see *Methods* 1.2 and 1.3):

$$s_R(t) \approx \sum_{j,k} {w_{jk}}^* \quad \psi_{jk}^{(\alpha)}(t) \tag{3}$$

In (3), which defines the synthesis of the rhythmic signal, indices j and k respectively label the scale and the time location of the wavelet. The parameter α characterizes the smoothness of the synthesis wavelet. This processing is only possible if the wavelet expansion of the original signal (4) can account for the presence of an arrhythmic 'β' exponent:

$$s(t) = \sum_{j,k} w_{jk} \;\; \psi_{jk}^{(\alpha+\beta^*/2)}(t) \tag{4}$$

The wavelet expansion of the original time series (4) and the synthesis of the rhythmic signal (3) rely on the use of two distinctive 'fractional spline wavelet' bases allowing to control for the differentiation of fractional order $\alpha + \beta^*/2$ and α (*Methods* 1.2). Ultimately, the resulting rhythmic time series $s_R(t)$ can be Fourier analyzed leading to the so-called *rhythms' spectroscopy* (Fig.2).

To illustrate the wavelet-RnB algorithm, we considered an alpha (10.5 Hz) oscillation in the background of a simulated arrhythmic time series (Fig.2A). This simulation was processed by wavelet-RnB to produce a rhythmic time series (Fig.2C). The arrhythmic drift which dominated the original time series (Fig. 2A) is removed in the reconstructed signal (Fig.2C). The spectral density of the rhythmic component provided with wavelet-

RnB (Fig.2D) exhibits a clear signature of the oscillation in comparison with the original Fourier spectrum (Fig.2B).

We further considered realistic simulations to assess wavelet-RnB estimations of both rhythmic and arrhythmic parameters (see methods 2.2 and Fig.M4 and M5). The simulations show that wavelet-RnB rhythmic amplitude and scaling exponents outputs are reliable to assess single or concurrent oscillations (sigma and delta), with minor caveats. First, rhythmic amplitude is slightly underestimated in arrhythmic conditions with high scaling exponents (Fig. M4B). Second, wavelet-RnB marginally overestimate the scaling exponents when a high amplitude oscillation is present (Fig. M4C). In both cases, the error from wavelet-RnB is marginal and represents less than 10% of the variance for either of their rhythmic or arrhythmic outputs.

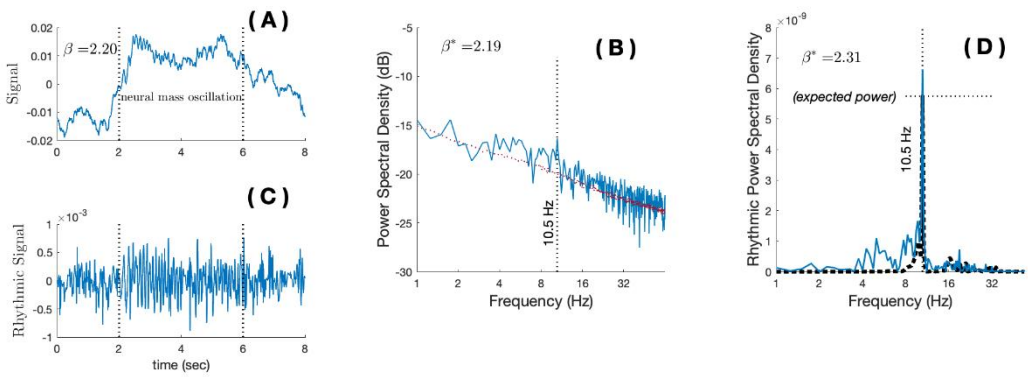

Fig.2. ***RnB* estimation in the wavelet domain.** **A.** Example of a simulated time series containing a mixture of a scale-free activity ($\beta = 2.2$; arrhythmic background) and an alpha oscillation (four seconds 10.5 Hz rhythm). **B.** The Fourier spectra of the original time series $s(t)$ displayed in (A), mostly dominated by the dominant arrhythmic background. **C.** The output $s_R(t)$ of the *RnB* algorithm, revealing the rhythmic features of the time series synthesized from the wavelet's coefficients filtered for the arrhythmic factor. **D.** The Fourier spectra of a single $s_R(t)$ epoch (in (C)) highlight a clear signature of the simulated oscillation that was added to the arrhythmic background, with a marginal "arrhythmic" contribution. This averaged across multiple epochs defining the rhythm's spectroscopy for further analyses (methods). The black dotted line is the original spectra of the simulated oscillation, without the addition of an arrhythmic background.

The spectroscopy of sleep recordings (511)

Given that rhythmic time series provided by wavelet-RnB are corrected for arrhythmicity, we demonstrated their potential to characterize transient rhythms during sleep. To do so, we used intracranial sleep recordings publicly available[18] (methods 3). Our analyses focused on the anterior cingulate and the precuneus, two key regions involved in sleep slow waves and sleep spindles, NREM delta and sigma rhythms[19,20]. Our main objective here is to show that rhythmic time series exhibit fundamental characteristics of NREM

sleep rhythms, notably their frequency content and inter-frequency coupling. To do so, we first evaluated how the rhythmic time series' spectroscopy provided a reliable representation of NREM cardinal rhythms as compared to spectral approaches. Second, we detected sleep slow waves in the intracranial rhythmic time series and investigated how these events locally group and synchronize other transient rhythms identified in each region's spectroscopy. Finally, we investigated the coupling between delta and sigma rhythms both in the rhythmic and original time series.

To better interpret our spectroscopy of NREM sleep recordings, we first illustrated how the NREM sleep power spectrum is decomposed using spectral methods such as FOOOF[12] and spectral-RnB. We then assessed the innovative contribution of the spectroscopy provided by wavelet-RnB. As expected, NREM2 and NREM3 sleep spectra were characterized by a 1/f arrhythmic background alongside sigma peaks (Fig.3A1 and A2). FOOOF confirmed such significant peaks in the average NREM spectrum in both stages and regions, with an additional theta peak in the precuneus during NREM2 and NREM3 sleep (Fig.3B1 and B2). Interestingly, spectral-RnB, upon which wavelet-RnB builds, revealed overlapping distributions of scaling exponents during NREM2 and NREM3 sleep, highlighting that a single exponent per stage (as parametrized by FOOOF) cannot account for the variety of arrhythmic regimes during NREM sleep (Fig.3C1 and C2). Additionally, spectral-RnB rhythmic outputs showed a sigma peak in each region during NREM2 and NREM3 sleep (Fig.3D1 and D2). Neither spectral-RnB or FOOOF revealed delta peaks below 4Hz, which fits with previous findings indicating the limitations of spectral parametrization methods to identify delta residual spectral power [21].

Next, we assessed whether wavelet-RnB spectroscopy provides a reliable representation of NREM cardinal rhythms. Interestingly, the NREM spectroscopy highlighted higher delta power in NREM3 as compared to NREM2 sleep, although the specific frequency bands varied between both regions (Fig.4A1 and A2). In the anterior cingulate, a low-frequency delta rhythmic peak ($1.17Hz$) predominated in NREM3 as compared to NREM2 sleep, whereas two delta rhythmic delta peaks (1.95 and 3.71 Hz) were found in the precuneus during NREM3 and NREM2 sleep. A rhythmic theta peak ($\approx 7Hz$) was also found specifically in the precuneus during NREM2 and NREM3 sleep. Additionally, rhythmic sigma peaks were found in both regions, with slightly faster frequencies in the anterior cingulate (12.5 Hz) as compared to the precuneus (13.5 Hz) and lower maximal power in NREM3 compared to NREM2. Wavelet-RnB also provided distributions of scaling exponents β in each region (Fig.4B1 and B2), with higher persistence in NREM3 as compared to NREM2 sleep in both regions. Thus, the wavelet-RnB spectroscopy reveals a more exhaustive NREM sleep spectral content as compared to spectral methods.

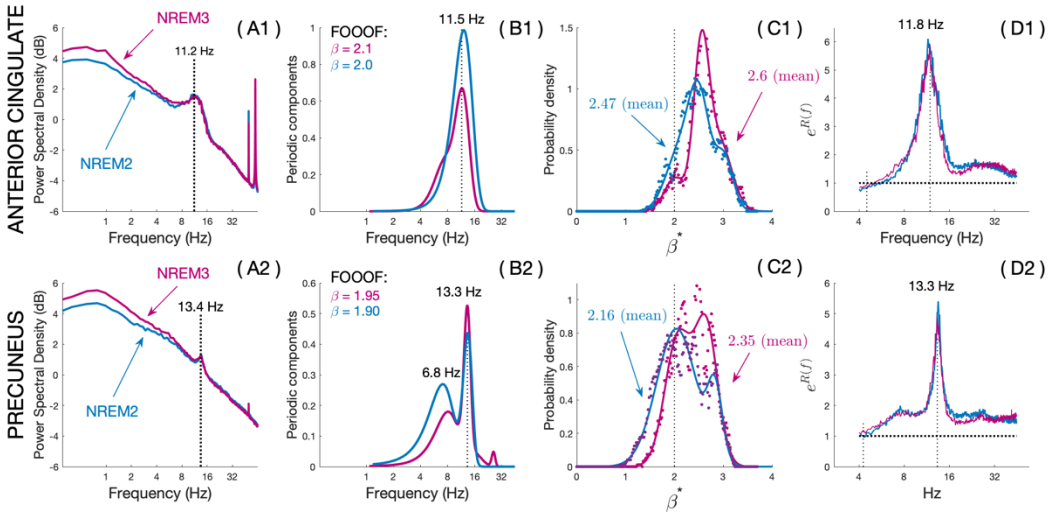

Fig.3. **FOOOF and spectral-*RnB* outputs during NREM sleep**. Results from spectral factorization during NREM sleep in the anterior cingulate (top row) and precuneus (bottom row). **A1, A2.** Standard spectral density per region in NREM2 (blue) and NREM3 (pink) sleep, highlighting a significant arrhythmic 1/f background alongside spectral peaks. **B1, B2.** Residual periodic power estimated by FOOOF in NREM2 and NREM3 sleep. **C1, C2**. Probability density of observed scaling exponents as assessed by spectral-*RnB* between epochs during NREM2 and NREM3. **D1, D2.** Spectral-*RnB* outputs residual rhythmic power, highlighting distinctive peaks in each region. Dashed horizontal lines indicate the threshold above which rhythmic activity stands out from the background. Dashed vertical lines indicate found spectral peaks.

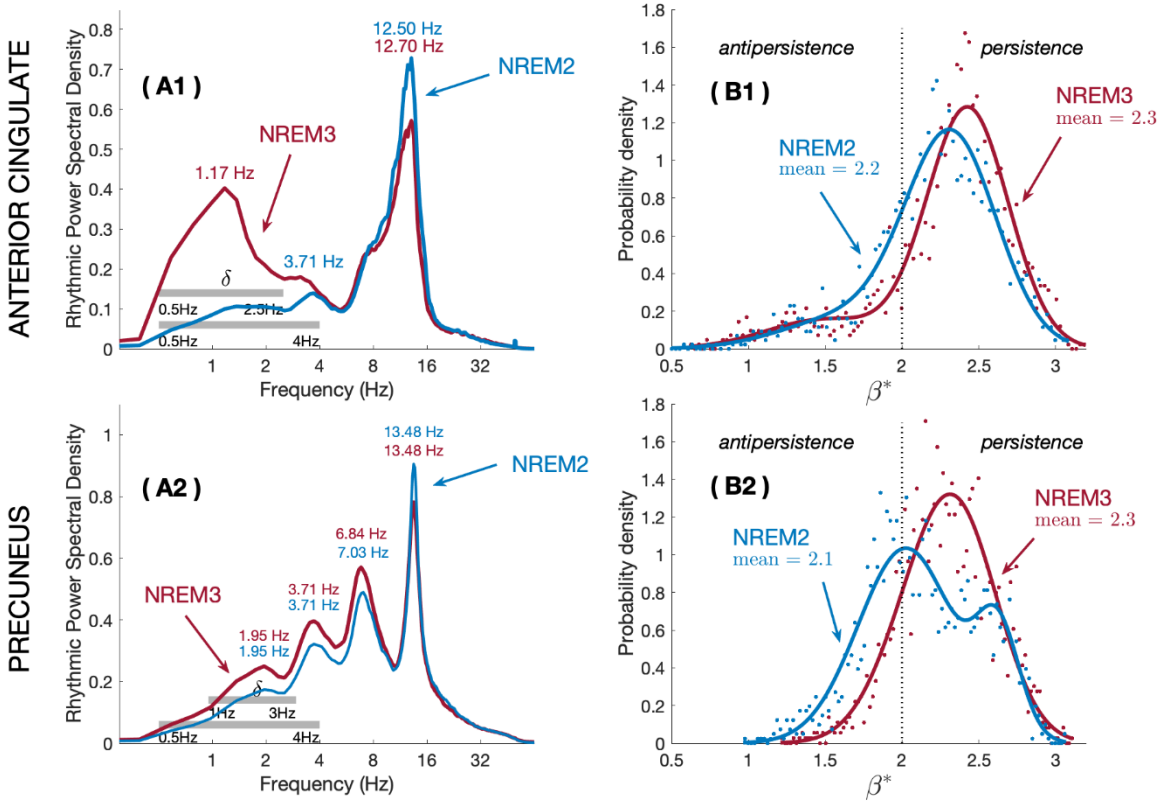

Fig.4. **Sleep spectroscopy from wavelet-*RnB* in the anterior cingulate and in the precuneus (NREM2 and NREM3 sleep stages). A1, A2.** The spectroscopy of NREM rhythmic time series exhibits a more detailed frequency content as compared to spectral methods, with peaks in expected frequencies that are associated with NREM sleep rhythms during NREM2 (blue) and NREM3 (red) in the anterior cingulate (**A1**) and precuneus (**A2**). The horizontal gray lines indicate the frequency bands that will define the SSWs detection in the next section. **B1, B2.** Scaling exponents as estimated from wavelets coefficients show distinctive distribution in each sleep stage and region. Individual NREM sleep epochs are represented with dots. Lines represent a mixture of Gaussian fit and mean exponents are indicated.

Rhythmic sleep slow waves modulate rhythmic and arrhythmic activity (333)

As wavelet-RnB spectroscopy revealed local delta peaks, we sought to detect SSWs in the rhythmic time series and to assess how they modulate other NREM rhythms. We adapted a SSWs' detector validated for intracranial recordings[22]. A two-pass was performed to provide a local inventory of rhythmic SSWs using the local features of each region's spectroscopy. A first 'standard' detection used the SSWs frequency band (0.5-4 Hz). It was followed by a second 'local' pass using the lower-frequency rhythmic delta peak that stood out locally in NREM3, the anterior cingulate ($[0.5-2.5]\ Hz$), and in the precuneus ($[1-3]\ Hz$), as depicted by the gray bars in Fig.4A1 and A2. The final

‘rhythmic SSWs’ (rSSWs) inventory is the nonredundant union of the ‘standard’ and ‘local’ detections in each region (methods 3.1).

The analysis of rSSWs showed an expected biphasic shape, with a suppression of higher frequency during their downstate (Fig.5A1 and A2; Fig. M6). Although the number of detected rSSWs was lower than in the original signal (see methods), rSSWs’ density was higher in NREM3 (5.5 and 5.6/min) compared to NREM2 (3.2 and 3.6/min) respectively for the anterior cingulate and precuneus. For all further analyses, we focused on NREM3 sleep predominantly as there is higher density of rSSW in this stage. Results from NREM2 were mostly similar (extended figure 5-1).

Spectroscopy-based analyses of rSSWs were done to assess how rSSWs transiently modulate rhythmic and arrhythmic activity during NREM3 sleep. As compared to baseline NREM epochs (without rSSWs; methods; Fig.5B1 and B2), most epochs with rSSWs had lower scaling exponents (lower persistence), although this effect was predominant in the anterior cingulate. Epochs with rSSWs also showed higher delta and lower sigma rhythmic power than baseline epochs in both regions, although the anterior cingulate showed a stronger increase in rhythmic delta and a widening of rhythmic sigma (Fig.5C1 and C2). The theta peak previously observed in the precuneus (Fig.4A2) also showed lower power during rSSWs as compared to the baseline. Results for NREM2 sleep were mostly similar (Extended-Fig. 5-1).

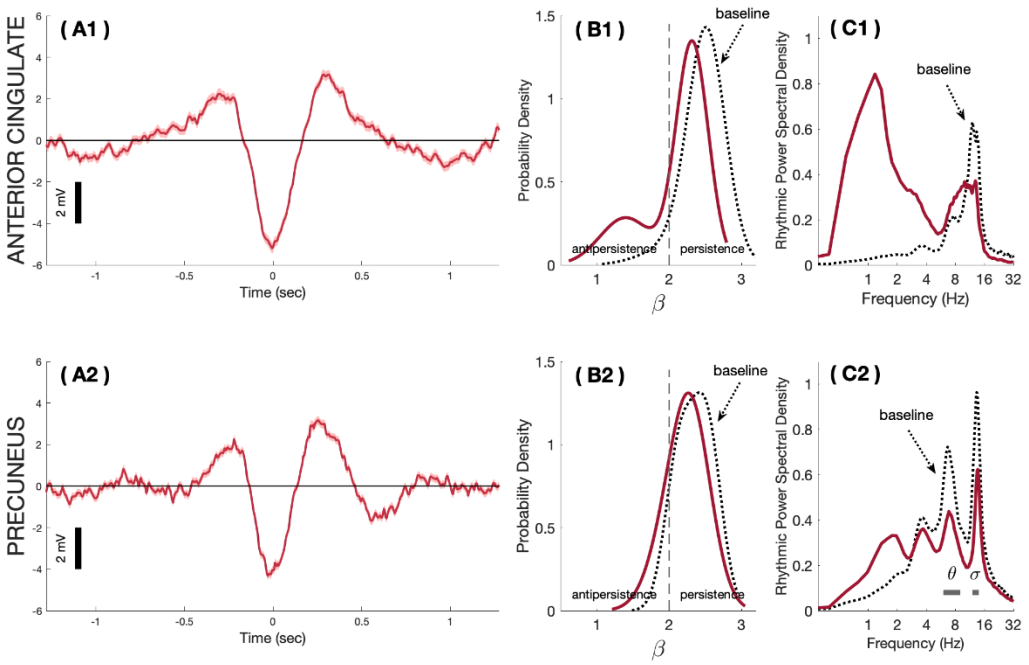

Fig.5. **SSWs in rhythmic time series from the anterior cingulate (top) and precuneus (bottom)**. **A1, A2.** Average waveforms of rSSWs detected during NREM3 in the anterior cingulate (top) and precuneus (bottom). **B1,B2.** Distribution of scaling exponents across epochs with rSSW (plain) and without rSSW (dashed lines). **C1,C2.** Spectroscopy of epochs with rSSWs (plain) and without rSSWs (dashed lines) during NREM3 sleep (the NREM2 case is in the supplementary material).

The spectroscopy of SSWs differ according to their transition period (208)

SSWs can be categorized as slow or fast switchers, depending on the duration of the *transition period* between their hyperpolarization and depolarization phase[23]. Interestingly, sigma rhythms are preferentially nested in the transition of slow switchers as compared to fast switchers during NREM sleep[24]. We thus considered whether this difference between slow and fast switchers could also be found in the rhythmic time series and in their spectroscopy.

We categorized each rSSW during NREM3 as a rhythmic slow switcher (rSlowS) or rhythmic fast switcher (rFastS; methods 3.2). We reproduced the clustering of rSSWs between rSlowS and rFastS in the rhythmic time series, with a distribution skewed toward rFastS in both regions (Fig.6A1 and A2). The spectroscopy of rSlowS differed from rFastS specifically in the anterior cingulate. In this region, rSlowS showed a bimodal distribution of scaling exponents with persistent and antipersistent modes, whereas rFastS showed a distribution of scaling exponents with a clear persistent mode (Fig.6C1; Wilcoxon test : z-statistic: -4.49, $p<0.001$). Compared to rFastS, rSlowS showed significantly higher rhythmic delta and higher rhythmic sigma power only in the anterior cingulate (Fig.6D1, t-test $p<0.05$). In the precuneus, arrhythmic and rhythmic estimates were superposable between rFastS and rSlowS (Fig.6C2 and D2). Similar findings were observed in NREM2 (Extended-Fig. 6-1).

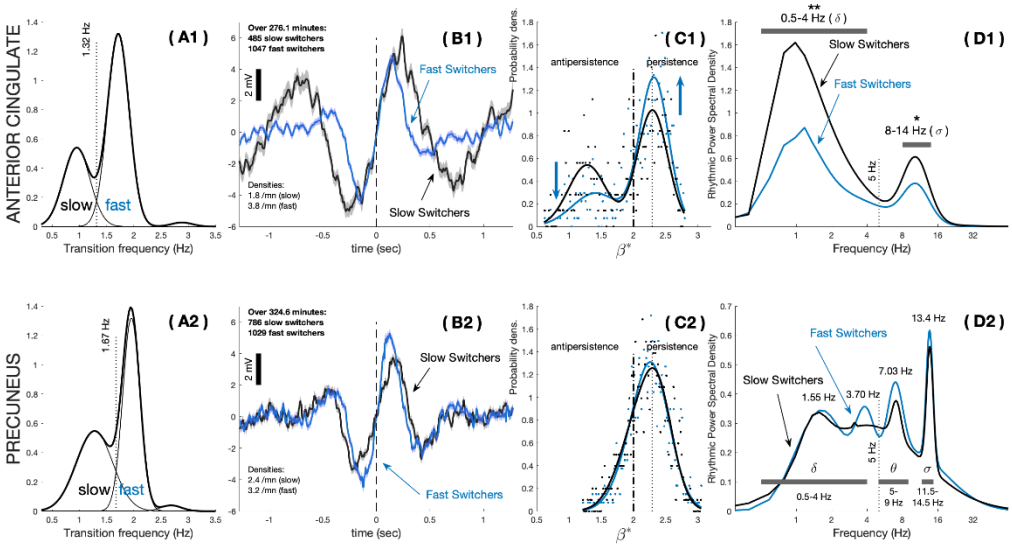

Figure 6. **The spectroscopy of slow (rSlowS) and fast switchers (rFastS) during NREM3. A1, A2.** The probability density of rSSWs according to their transition frequency is shown for the anterior cingulate **(A1)** and precuneus **(B1),** highlighting a bimodal distribution in both regions. The transition frequency to define rFastS and rSlowS is shown as a dashed vertical line. **B1, B2**. Average waveform of rSlowS and rFastS, with respect to the separation frequency are defined in A1 and A2 respectively. Averages are centered around the zero-crossing markers. **C1, C2.** Probability density of the scale-free exponents is estimated by Wavelet-*RnB* for rSlowS and rFastS in each region. **D1, D2.** Spectroscopy of the rhythmic switchers in NREM3 are shown for both regions. The horizontal bold vertical bars depict local frequency bands which were considered for further PAC analyses. Bilateral T-tests were performed in each region to investigate switcher-related differences in the integrated rhythmic power (for each bolded frequency bands, delta, and sigma in the anterior cingulate; delta, theta, and sigma in the precuneus). Significance is depicted using stars (p-values: * <0.05; **<0.01).

Rhythmic slow and fast switchers regroup transient sigma and theta rhythms (246)

To evaluate how rSSWs synchronize NREM rhythms with respect to their transition period, we assessed the scalograms of rSlowS and rFastS derived from the rhythmic time series (Fig.7 for NREM3 and Fig.7-1 for NREM2). Induced and phase-locked rhythmic power were both considered to assess in the time domain how rSSWs group or synchronize rhythmic activity, respectively. Whereas induced power is the cumulant of the amplitude at each timepoint regardless of the phase of the rhythmic signal, phase-locked power is sensitive to the in-phase synchrony of the rhythmic signal across rSSWs[25]. As sigma rhythms occur during the transition of rSlowS specifically from hyperpolarization to depolarization[24], we hypothesized that rSlowS would show higher phase-locked sigma power during their transition as compared to rFastS.

Induced sigma power was observed across rSlowS and rFastS in both regions (Fig.7A1, A2, C1, C2). The precuneus also showed induced theta power around the transition phase of rFastS and rSlowS (Fig.7A2, C2). As expected, rSlowS in the anterior cingulate showed phase-locked sigma rhythmic power in their transition, with increasing frequency and reaching maximal power synchronously with their depolarizing peak (Fig.7 B1). Although induced 'theta bursts' in the precuneus were not sufficiently synchronized around the transition to produce a theta signature in the locked scalogram, phase-locked rhythmic sigma power occurred later with a delay around 400 msec, preferentially for rFastS (Fig.7B2, D2). In NREM2 sleep, induced sigma and theta rhythmic powers were observed for both switchers, although rhythmic sigma activity was not synchronized (Extended-Fig. 7-1).

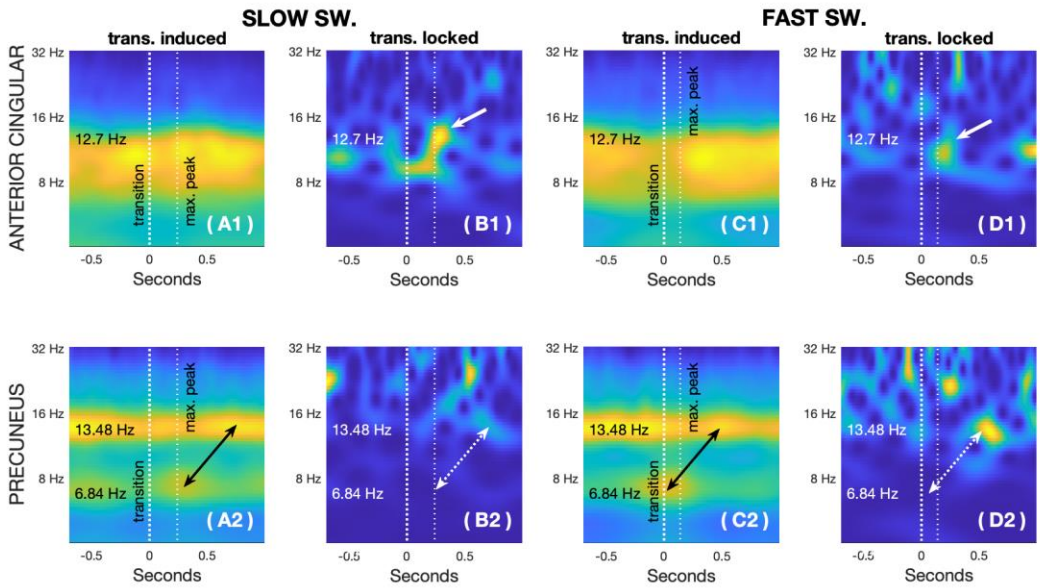

Fig.7. **Induced and phase-locked rhythmic power synchronized with the transition of rSlowS and rFastS during NREM3 sleep.** Scalograms of induced (**A1, A2, C1, and C2**) and phase-locked (**B1, B2, D1, and D2**) power for the rSlowS (Left panels) and the rFastS (Right panels), co-registered around their zero crossing, in the anterior cingulate (top panels) and the precuneus (bottom panels). The 'induced' scalograms are the average wavelet power whereas the 'locked' scalograms are the power of the average across the wavelet transform in the rhythmic time series. Vertical lines indicate the transition markers for rSlowS and rFastS (zero-crossing in bold; the depolarization 'max. peak' as estimated from the averaged signal in Fig.7 B1 and B2). The arrows in top panels (anterior cingulate) indicate phase-locked power around the transition of rSlowS, whereas arrows in bottom panels (precuneus) emphasize the temporal relationship between the induced theta and phase-locked sigma activity. Each plane is individually normalized for visualization (hot colors for higher power).

Slow switchers and theta bursts can promote SSW-sigma coupling in rhythmic time series (454)

To evaluate how sigma amplitude is systematically modulated by the phase of delta rhythms in NREM sleep, we computed delta-sigma phase-amplitude coupling (PAC) during SSWs. We considered events detected in the rhythmic time series (rhythmic PAC: rPAC) and in the original EEG signal (PAC). rPAC was computed using delta frequencies which stood out locally in each region's spectroscopy (Fig. 6), whereas PAC was computed using standard SSW (0.5-4Hz) and sigma (12-16Hz) frequencies. We hypothesized higher PAC for rSlowS and rFastS detected in the rhythmic time series as compared to events detected in the original signal since arrhythmic interferences should be minimized. We also hypothesized higher PAC for slow as compared to fast switchers predominantly in the rhythmic as compared to the raw time series.

As shown in Fig.8 (A and B), rPAC values were significantly higher than PAC values for both types of switchers in the two brain regions (Mann-Whitney U-tests: $p < 0.001$ for all events in NREM2 and NREM3, supplementary table 1). These results suggest that phase interferences are reduced in the rhythmic time series, revealing strong phase coupling between delta and sigma rhythms.

Additionally, rPAC was significantly higher for rSlowS as compared to rFastS in the anterior cingulate during NREM3 (Fig. 8A, NREM3: U=2.82, p=0.005; NREM2: U=0.78, p=0.4), as expected. This difference between SlowS and FastS was not significant with standard PAC in the anterior cingulate (NREM3: U= 1.85, p-value=0.06; NREM2: U= 1.23, p=0.21). In the precuneus, no significant differences in rPAC were found between switchers (Fig. 8B, NREM3: U=0.18, p>.9; NREM2: U=1.59, p=0.13).

Since previous literature suggests that NREM theta bursts (TBs) precede slow-wave-spindle complexes and facilitate delta-sigma PAC[26], we explored the effects of theta bursts on rPAC during rSSWs in the precuneus. This analysis is prompted by the specific theta peak and induced theta found in the precuneus spectroscopy (Fig.4) and with the transition of rSlowS and rFastS in the precuneus scalogram analyses (Fig.7). We designed a rhythmic TBs detector that used the specific theta peak found in the precuneus spectroscopy. Then, we identified rSSWs co-occurring with TBs (<500ms; rSSWs+TBs events) and rSSWs that did not (rSSWs-TBs). We hypothesized higher delta-sigma rPAC for rSSWs+TBs events as compared to rSSWs-TB in the precuneus.

As shown in Fig.8C, delta-sigma rPAC was higher for rSSWs+TBs compared to rSSWs-TBs specifically during NREM3 (NREM3: U=2.46, p=0.01; NREM2: U=1.61, p=0.11). Importantly, rSSW+TBs events represented around 10% of all rSSWs in NREM2 (119/1188 rSSWs) and around 6% of all rSSWs in NREM3 (116/1815 rSSWs). Thus,

although rSSW+TBs are rare, they constitute a significant modulator of rPAC in NREM3. Thus, the rhythmic time series shows globally higher delta-sigma coupling. rPAC was higher for rSlowS in the anterior cingulate and was significantly amplified with TBs in the precuneus.

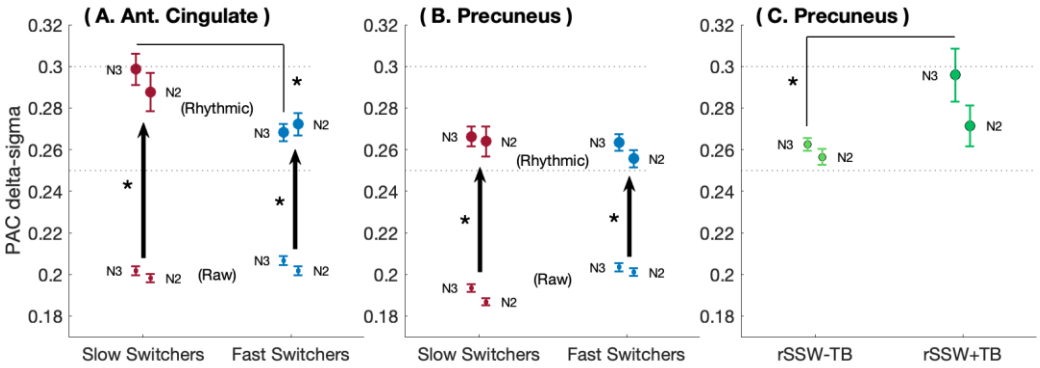

Fig.8. Delta-sigma PAC from original and rhythmic time series associated with slow and fast switchers and rSWS with and without TBS. Average values and standard error of the mean for rPAC (rhythmic) and PAC (raw), for slow (red) and fast (blue) switchers during NREM2 (N2) and NREM3 (N3) sleep in the anterior cingulate (A) and in the precuneus (B, C). In the precuneus, rPAC values are shown for all rSSWs without TBs (rSSW-TBs) and for rSSWs co-detected with a TBs (rSSW+TBs). For each event type, arrows indicate significant differences between PAC and rPACs values (significant differences both in NREM2 and NREM3). Brackets indicate a significant difference between event types in each sleep stage. Stars indicate significance value (*: p≤0.01).

Discussion (1557)

Interference between background activity and neurophysiological rhythms in the time domain is a challenge that current spectral parametrization methods cannot address[13]. We introduce a wavelet-based method able to disentangle the rhythmic time-series from the arrhythmic background. Rhythmic time series disclose cardinal NREM sleep rhythms and enhanced the sensitivity to their mutual coupling.

Wavelet-RnB allows time-domain analyses of brain rhythms free from arrhythmicity, whereas spectral methods focus on properties of “periodic” peaks and aperiodic background[12,13]. Usually characterized as a spectral 1/f slope (i.e., a scaling exponent), arrhythmicity is expressed by dynamical scale-free fluctuations unrelated to specific oscillations. As an example, a “pure arrhythmic” EEG (i.e., without cardinal oscillations) represents around 80% of the recording time in NREM2 and more than 50% in NREM3 sleep[5]. This ubiquitous background can bias spectral and temporal estimates of brain rhythms: time series with higher scaling exponents show longer range dependencies

characterized by slower fluctuations contributing to delta power in standard spectral analyses and which may also be confounded for slow waves [14,21]. As previously observed[8,27], our results showed higher scaling exponents in deeper NREM sleep in both cerebral regions of interest. We also showed that scaling exponents fluctuate across sleep epochs, a finding which was previously reported by studies using multifractal analyses[28]. This variability may reflect time-dependent changes in the excitation-inhibition balance, postsynaptic properties, and in the dynamics of circuit activities during sleep [29–31]. However, arrhythmic differences between sleep stages and epochs may bias amplitude and phase estimates of oscillatory activity[14]. By extracting rhythmic time series corrected for arrhythmicity, wavelet-RnB can isolate transient NREM sleep oscillations while controlling 'instantaneously' for differences in arrhythmic backgrounds.

Recent simulation studies pinpointed limitations in spectral methods to reveal low frequency rhythmic delta power due to interferences between arrhythmicity and low frequency rhythms in the Fourier domain [21]. Hence, previous sleep studies using such methods mostly focused on sigma periodic peaks[9,27,32]. Our spectral variant of RnB also failed to reveal residual rhythmic delta power in NREM sleep. However, our simulations showed that wavelet-RnB can robustly estimate delta and sigma rhythms across different scale-free scenarios, with a slight underestimation of sigma power concomitant with higher scaling exponent - which is also an issue for spectral parametrization methods [21]. Compared to its spectral variant, wavelet-RnB detected delta, theta, and sigma differences between NREM2 and NREM3 in the anterior cingulate, which correspond to changes expected in NREM sleep [33]. We argue that the improved sensitivity of wavelet-RnB is granted by the wavelet based arrhythmic 'punctual' estimations and corrections in the time-scale domain as compared to the Fourier spectral domain (methods). In comparison with spectral approaches, wavelet-RnB estimates 'β' in the "time-scale" domain (methods 1.2) are less likely to be biased by the overlap between rhythmic low frequencies and arrhythmic fluctuations. This time-scale approach also accounts for the nonstationary nature of cerebral electrophysiological activity, which allows to perform a reliable spectroscopy and time-domain analyses of brain rhythms. As a proof-of-concept, we detected SSWs in the rhythmic time series (rSSWs) using spectroscopy-adapted criteria in accordance with recent guidelines to adapt detection criteria to local frequency content[14,34]. As expected, rSSWs showed bimodal waveform and modulated the sigma power differentially in the two brain regions[35,36]. Moreover, clustering based on the bimodal transition of rSSWs was able to reproduce the 'fast-slow' switchers classification of the rSSWs, as already found on the scalp EEG sleep recordings[23,35].

As compared to the precuneus, the anterior cingulate spectroscopy showed stronger differences in arrhythmic and rhythmic activities between NREM2 and NREM3 and in rSSWs vs. baseline. In the anterior cingulate specifically, NREMs showed higher rhythmic

delta power in NREM3 as compared to NREM2 sleep, in accordance with the well-known anterior predominance of NREM delta power and of SSWs [37,38]. Furthermore, higher rhythmic delta power and lower scaling exponents were observed during transient rSSWs as compared to baseline. The anterior specificity of these differences may reflect the cortico-genesis of the SSWs, since SSWs originate in the anterior cingulate before spreading in other regions[20]. Interestingly, lower scaling exponents during rSSWs in the anterior cingulate resonate with a recent study reporting a flatter slope (lower scaling exponent) during the depolarization phase of SSWs in anterior regions[31]. Higher delta activity and lower scaling exponents during rSSWs can be interpreted as an increase of local neural synchrony and changes in the excitatory-inhibitory balance occurring predominantly during anterior SSWs.

Our results also showed several differences between rSlowS and rFastS in the anterior cingulate. First, rSlowS had higher delta and sigma rhythmic power and lower scaling exponents as compared to rFastS. Previous research indicated that slow switchers show a longer depolarization period and a larger amplitude than fast switchers, suggesting higher underlying neural synchrony during these events[35,37]. Lower scaling exponents during rSlowS could represent higher excitatory drive as neurons are depolarized synchronously during the slow oscillation[7]. Higher sigma activity during rSlowS also fits with the idea that SSWs with longer transition are promoters of higher thalamo-cortical connectivity that supports cortical sigma synchronization and sleep spindles occurrence[23,26,39–41]. Second, rSlowS in the anterior cingulate were associated with sigma rhythmic phase-locked power specifically after the transition (zero crossing) to the depolarization peak. These results corroborate a previous study indicating that sleep spindles in anterior regions occur specifically during the depolarizing phase of slow switchers, whereas there was no phase relationship with fast switchers[35]. Finally, rSlowS also showed higher delta-sigma PAC than rFastS in the anterior cingulate. Interestingly, a previous study showed that slow switchers specifically coupled to sleep spindles promote stronger EEG frontal connectivity across their depolarization phase [23]. Importantly, arrhythmic properties were recently found to be related with local properties contributing to network dynamics and long-range connectivity[5]. Thus, our results about lower scaling exponents and higher sigma PAC during rSlowS in the anterior cingulate lead us to hypothesize that arrhythmic antipersistence facilitate the emergence of a cortico-cortical network involving the anterior cingulate during coupled rSSWs-sleep spindles complexes.

Motivated by the singular theta peak found in the precuneus NREM's spectroscopy and by the fact that induced theta was found to precede rSSW phase-locked sigma, theta bursts (TBs) were inventoried (Fig.8, also see Fig.M7). Crucially, co-occurrence of TBs with rSSWs resulted in higher delta-sigma PAC. Our results are supported by recent

findings which identified TBs as an “early” down state which could facilitate slow waves up states, sigma synchronization and sleep spindles occurrence, particularly when the slow oscillation is less synchronized[26,42]. Thus, whereas sigma synchronization could be promoted by rSlowS and the antipersistent arrhythmic background in anterior regions, TBs could be necessary to drive sigma synchronization in posterior regions where slow oscillations are less synchronized. Although distinct from sleep spindles, one can hypothesize that transient sigma rhythms occurring during rTBs or rSlowS can synchronize across brain regions to form “global” spindles. Interestingly, a MEG study showed that EEG “global” spindles initially involve local synchronized sigma activity in precuneus, which extends only later in the anterior cingulate [19]. We thus propose that transient rhythmic sigma events observed during rSlowS and TBs underlie the emergence of the spindles subset which are coupled to slow waves[35].

Delta-sigma PAC was higher for SSWs detected in the rhythmic as compared to the original signal. A few reasons could account for this. First, it is possible that the spectroscopy-improved rSSW detection criteria increased the representation of genuine slow oscillations, which led to better disclose delta-sigma coupling[43]. Similarly, the use of the delta rhythmic peak (as compared to standard slow-wave activity) as a detection criterion of rSSWs might also have increased the PAC, since lower frequency SSWs lead to higher PAC estimates[44]. Finally, the rhythmic time series might better estimate the inherent phases of the cardinal rhythms, as arrhythmic interferences have been attenuated [14]. In any case, it is likely that coupling in the rhythmic time series provides a better insight into the oscillatory-dependent hippocampo-thalamo-cortical interactions altered in numerous disease processes[4,45]. Currently, PAC metrics express high heterogeneity and are often low, preventing their clinical use[46]. By jointly improving the detection of NREM rhythms and the assessment of their coupling, wavelet-RnB could decrease the heterogeneity of PAC or phase-based metric findings.

Wavelet-RnB represents a significant paradigm shift in EEG spectral analysis. It constitutes a crucial step forward towards disentangling electrophysiological rhythms from arrhythmicity when it comes to time series. Although fractional spline wavelets used by RnB are specifically geared towards a robust scale-free estimation which helped whiten our signal in the time-frequency domain[47], further refinements could help to estimate rhythmic processes even more precisely. Specifically, our current rhythmic signal may not be considered as a “sparse representation” in terms of oscillatory transient events. Although we used a shrinkage approach to smooth spurious fluctuations, future work could improve this process to better exploit the rhythmic time series. For instance, instead of using standard detection criteria into the rhythmic time series, previously proposed matching pursuit methods could be applied to the rhythmic signal to better identify basic patterns corresponding to NREM rhythms. This would allow the

development of detectors relaxing the need of prior detection criteria[16,48,49]. Alternatively, previously proposed cycle-by-cycle analysis could also be used directly in the rhythmic signal to identify periods where such events manifest[50]. In conclusion, we believe that the application and refinement of this '*sleep EEG spectroscopy'* alongside the rhythmic time series will provide a better understanding of rhythmic and arrhythmic processes in sleep and, more generally, in quantitative EEG analysis in various clinical conditions.

References

1. Buzsáki, G. Large-scale recording of neuronal ensembles. *Nat Neurosci* **7**, 446–451 (2004).

2. Helfrich, R. F. *et al.* Bidirectional prefrontal-hippocampal dynamics organize information transfer during sleep in humans. *Nat. Commun.* **10**, 3572 (2019).

3. Klinzing, J. G. *et al.* Spindle activity phase-locked to sleep slow oscillations. *NeuroImage* **134**, 607–616 (2016).

4. Helfrich, R. F., Mander, B. A., Jagust, W. J., Knight, R. T. & Walker, M. P. Old Brains Come Uncoupled in Sleep: Slow Wave-Spindle Synchrony, Brain Atrophy, and Forgetting. *Neuron* **97**, 221-230.e4 (2018).

5. Helfrich, R. F., Lendner, J. D. & Knight, R. T. Aperiodic sleep networks promote memory consolidation. *Trends Cogn. Sci.* **25**, 648–659 (2021).

6. He, B. J. Scale-free brain activity: past, present, and future. *Trends Cogn. Sci.* **18**, 480–487 (2014).

7. Gao, R., Peterson, E. J. & Voytek, B. Inferring synaptic excitation/inhibition balance from field potentials. *NeuroImage* **158**, 70–78 (2017).

8. Lendner, J. D. *et al.* An electrophysiological marker of arousal level in humans. *eLife* **9**, e55092 (2020).

9. Schneider, B. *et al.* Scale-free and oscillatory spectral measures of sleep stages in humans. *Front. Neuroinformatics* **16**, 989262 (2022).

10. Kozhemiako, N. *et al.* Sources of Variation in the Spectral Slope of the Sleep EEG. *eNeuro* **9**, ENEURO.0094-22.2022 (2022).

11. Hernandez, J. *et al.* EEG rhythmic and arrhythmic spectral components and functional connectivity at resting state may predict the development of synucleinopathies in idiopathic REM sleep behavior disorder. *SLEEP* zsae074 (2024) doi:10.1093/sleep/zsae074.

12. Donoghue, T. *et al.* Parameterizing neural power spectra into periodic and aperiodic components. *Nat. Neurosci.* **23**, 1655–1665 (2020).

13. Wen, H. & Liu, Z. Separating Fractal and Oscillatory Components in the Power Spectrum of Neurophysiological Signal. *Brain Topogr.* **29**, 13–26 (2016).

14. Donoghue, T., Schaworonkow, N. & Voytek, B. Methodological considerations for studying neural oscillations. *Eur J Neurosci* **55**, 3502–3527 (2022).

15. Jurkiewicz, G. J., Hunt, M. J. & Żygierewicz, J. Addressing Pitfalls in Phase-Amplitude Coupling Analysis with an Extended Modulation Index Toolbox. *Neuroinformatics* **19**, 319–345 (2021).

16. Durka, P., Dovgialo, M., Duszyk-Bogorodzka, A. & Biegański, P. Two-Stage Atomic Decomposition of Multichannel EEG and the Previously Undetectable Sleep Spindles. *Sensors* **24**, 842 (2024).

17. Schaefer, A., Brach, J. S., Perera, S. & Sejdić, E. A comparative analysis of spectral exponent estimation techniques for 1/fβ processes with applications to the analysis of stride interval time series. *J. Neurosci. Methods* **222**, 118–130 (2014).

18. Ellenrieder, N. *et al.* How the Human Brain Sleeps: Direct Cortical Recordings of Normal Brain Activity. *Ann. Neurol.* **87**, 289–301 (2020).

19. Zerouali, Y. *et al.* A time-frequency analysis of the dynamics of cortical networks of sleep spindles from MEG-EEG recordings. *Front Neurosci-switz* **8**, 310 (2014).

20. Murphy, M. *et al.* Source modeling sleep slow waves. *Proc National Acad Sci* **106**, 1608–1613 (2009).

21. Gerster, M. *et al.* Separating Neural Oscillations from Aperiodic 1/f Activity: Challenges and Recommendations. *Neuroinformatics* **20**, 991–1012 (2022).

22. Frauscher, B. *et al.* Facilitation of epileptic activity during sleep is mediated by high amplitude slow waves. *Brain* **138**, 1629–1641 (2015).

23. Bouchard, M. *et al.* Sleeping at the switch. *Elife* **10**, e64337 (2021).

24. Nicolas, J. *et al.* Sigma oscillations protect or reinstate motor memory depending on their temporal coordination with slow waves. *eLife* **11**, e73930 (2022).

25. Tallon-Baudry, C., Bertrand, O., Tallon-Baudry, C. & Bertrand, O. Oscillatory gamma activity in humans and its role in object representation. *Trends Cogn. Sci.* **3**, 151–162 (1999).

26. Gonzalez, C. E. *et al.* Theta Bursts Precede, and Spindles Follow, Cortical and Thalamic Downstates in Human NREM Sleep. *J. Neurosci.* **38**, 9989–10001 (2018).

27. Bódizs, R. *et al.* A set of composite, non-redundant EEG measures of NREM sleep based on the power law scaling of the Fourier spectrum. *Sci. Rep.* **11**, 2041 (2021).

28. Lina, J.-M., O'Callaghan, E. K. & Mongrain, V. Scale-Free Dynamics of the Mouse Wakefulness and Sleep Electroencephalogram Quantified Using Wavelet-Leaders. *Clocks Sleep* **1**, 50–64 (2019).

29. Niethard, N., Brodt, S. & Born, J. Cell-Type-Specific Dynamics of Calcium Activity in Cortical Circuits over the Course of Slow-Wave Sleep and Rapid Eye Movement Sleep. *J Neurosci* **41**, 4212–4222 (2021).

30. Alfonsa, H. *et al.* Intracellular chloride regulation mediates local sleep pressure in the cortex. *Nat. Neurosci.* **26**, 64–78 (2023).

31. Brake, N. *et al.* A neurophysiological basis for aperiodic EEG and the background spectral trend. *Nat. Commun.* **15**, 1514 (2024).

32. Horváth, C. G. *et al.* Overnight dynamics in scale-free and oscillatory spectral parameters of NREM sleep EEG. *Sci. Rep.* **12**, 18409 (2022).

33. Steriade, M. The corticothalamic system in sleep. *Front Biosci* **8**, d878-899 (2003).

34. Muehlroth, B. E. & Werkle‐Bergner, M. Understanding the interplay of sleep and aging: Methodological challenges. *Psychophysiology* **57**, e13523 (2020).

35. Chylinski, D. *et al.* Timely coupling of sleep spindles and slow waves linked to early amyloid-β burden and predicts memory decline. *eLife* **11**, e78191 (2022).

36. Klinzing, J. G., Niethard, N. & Born, J. Mechanisms of systems memory consolidation during sleep. *Nat. Neurosci.* **22**, 1598–1610 (2019).

37. Vyazovskiy, V. V., Riedner, B. A., Cirelli, C. & Tononi, G. Sleep Homeostasis and Cortical Synchronization: II. A Local Field Potential Study of Sleep Slow Waves in the Rat. *Sleep* **30**, 1631-S1 (2007).

38. Hubbard, J. *et al.* Rapid fast-delta decay following prolonged wakefulness marks a phase of wake-inertia in NREM sleep. *Nat. Commun.* **11**, 3130 (2020).

39. Cox, R., Rüber, T., Staresina, B. P. & Fell, J. Sharp Wave-Ripples in Human Amygdala and Their Coordination with Hippocampus during NREM Sleep. *Cereb. Cortex Commun.* **1**, tgaa051 (2020).

40. Rigas, P. & Castro-Alamancos, M. A. Thalamocortical Up States: Differential Effects of Intrinsic and Extrinsic Cortical Inputs on Persistent Activity. *J. Neurosci.* **27**, 4261–4272 (2007).

41. Botella-Soler, V., Valderrama, M., Crépon, B., Navarro, V. & Quyen, M. L. V. Large-Scale Cortical Dynamics of Sleep Slow Waves. *PLoS ONE* **7**, e30757 (2012).

42. Jiang, X., Gonzalez-Martinez, J. & Halgren, E. Posterior Hippocampal Spindle Ripples Co-occur with Neocortical Theta Bursts and Downstates-Upstates, and Phase-Lock with Parietal Spindles during NREM Sleep in Humans. *J. Neurosci.* **39**, 8949–8968 (2019).

43. Aru, J. *et al.* Untangling cross-frequency coupling in neuroscience. *Curr. Opin. Neurobiol.* **31**, 51–61 (2015).

44. Steriade, M. Grouping of brain rhythms in corticothalamic systems. *Neuroscience* **137**, 1087–1106 (2006).

45. McConnell, B. V. *et al.* The aging slow wave: a shifting amalgam of distinct slow wave and spindle coupling subtypes define slow wave sleep across the human lifespan. *SLEEP* **44**, zsab125 (2021).

46. Mander, B. A., Winer, J. R. & Walker, M. P. Sleep and Human Aging. *Neuron* **94**, 19–36 (2017).

47. Blu, T. & Unser, M. The fractional spline wavelet transform: definition end implementation. *2000 IEEE Int. Conf. Acoust., Speech, Signal Process. Proc. (Cat 00CH37100)* **1**, 512–515 vol.1 (2000).

48. Durka, P. J. & Blinowska, K. J. Analysis of EEG transients by means of matching pursuit. *Ann. Biomed. Eng.* **23**, 608–611 (1995).

49. Krstulović, S. & Gribonval, R. MPTK: Matching Pursuit Made Tractable. *2006 IEEE Int. Conf. Acoust. Speech Signal Process. Proc.* **3**, III-496-III–499 (2006).

50. Cole, S. & Voytek, B. Cycle-by-cycle analysis of neural oscillations. *J. Neurophysiol.* **122**, 849–861 (2019).

Methods

This section describes methodological steps that support the present work. All subsections indicated with a * are associated with numerical resources available on a public repository (GitHub), with examples and preprocessed data allowing to reproduce the figures with comments.

*1.1 The Spectral – RnB**

The spectral factorization (1) is a multiplicative model of the power spectrum accounting for the combination of arrhythmic and rhythmic processes. Expanding the exponential factor, this product can eventually accommodate an additive model,

$$\Gamma(f) \approx \frac{c}{f^{\beta}} + c\, f^{-\beta} R(f) + \cdots \tag{5}$$

where the first term accounts for the arrhythmic background, and the second term is a resonance if $R(f)$ is sufficiently decaying at low frequency to compensate the infrared divergence. This expansion can explain the possible modulation of narrow band power peaks. To extract the arrhythmic factor, we follow the IRASA approach[13], considering the power spectrums obtained from a series of rescaling transforms $f \to af$,

$$\Gamma(f) = \frac{c}{f^{\beta}}\, e^{R(f)} \;\to\; \Gamma_a(f) = \frac{c}{f^{\beta}}\, a^{-\beta}\, e^{R(af)} \tag{6}$$

where $0 < a < 2$ is chosen in pair, a and $1/a$. Then, from a n randomly selected values for a, the geometric average

$$Q(f) = \left(\prod_{a_1}^{a_n} \Gamma_a(f)\, \Gamma_{1/a}(f) \right)^{\frac{1}{2n}} = P(f)\, e^{\mathcal{E}(f)} \tag{7}$$

exhibits the arrhythmic factor $P(f) = c/f^{\beta}$ since a random rescaling will not preserve narrowband rhythmic processes present in the spectrum and consequently $\mathcal{E}(f) = 1/2n \sum_{a_i} \big(R(a_i f) + R(a_i^{-1} f) \big) \approx 0$. Thus, $Q(f)^{-1} \approx P(f)^{-1}$ is a spectral filter for each epoch able to whiten the individual power spectrums to be averaged in (2). This epoch-wise filtering technique is the core of the spectral-RnB algorithm.

1.2 The Wavelet – RnB: Estimation of the scaling exponent*

A uniform self-similarity cannot fully account for the scale-free dynamics of neural activity[51]. However, we assume that self-similarity and a second-order statistics of the signal's fluctuations are suitable at the timescale of each epoch. The scale-free properties can however vary between epochs. This corresponds to a local linearization (additive model) of the underlying arrhythmic and rhythmic processes. Thus, assuming a unique scaling exponent for each 4 second epoch, we consider robust estimator of the β exponent from a discrete wavelet decomposition of the signal,

$$s(t) = \sum_j \sum_{k=1}^{n_j} w_{j,k} \;\; \psi_{j,k}^{(\alpha)}(t) \tag{8}$$

In this expansion, the wavelet $\psi_{j,k}^{(\alpha)}(t)$ is a 'transient little wave' (see Fig.M1A) with a temporal scale $\approx 2^j$ and located at $t = k\,2^j$ where k and j are integer,

$$\psi_{j,k}^{(\alpha)}(t) = 2^{-\frac{j}{2}}\,\psi^{(\alpha)}\left(2^{-j}\,t - k\right)$$

The smoothness of the 'mother wavelet' $\psi^{(\alpha)}(t)$ is controlled by the regularity parameter α. This 'little wave' oscillates with a frequency f_0 that depends on the parameter α. Therefore, the main frequency of the wavelets at scale j in expansion (8) is $\approx 2^{-j}\,f_0$. The figure Fig.M1A illustrates an example of this kind of wavelets and the multiresolution 'time-scale' representation of a signal in such a basis is illustrated in Fig.M1C.

The log-log regression allowing to estimate the scaling exponents in the spectral domain $\log\Gamma(f) \approx -\beta \log f$ can be reformulated in the wavelet domain[52] as:

$$\beta^* = \frac{\sum_{j_1}^{j_2} n_j \sum_{j_1}^{j_2} j\, n_j\, D_j - \sum_{j_1}^{j_2} j\, n_j \sum_{j_1}^{j_2} n_j\, D_j}{\sum_{j_1}^{j_2} n_j \sum_{j_1}^{j_2} n_j\, j^2 - \left(\sum_{j_1}^{j_2} j\, n_j\right)^2} \tag{9}$$

with the second-order statistics

$$D_j = \log\left(\frac{1}{n_j}\sum_k {w_{j,k}}^2\right)$$

The regression, illustrated on Fig.MD is done across scales ranging from j_1 (high frequencies) to j_2 (low frequencies). Importantly, this β^* estimate in the "time-scale" domain is less likely to be biased by the presence of transient oscillations and specific peaks in the Fourier domain as described in [21]. This is because this regression relies on "transient" fluctuations, mostly dominated by the scale-free background in periods when oscillations are and are not present. Thus, the range from j_1 (high frequencies) to j_2 (low frequencies) should cover the spectral domain of interest with respect to the rhythms to be further extracted. This estimate must also be reliable with respect to the second order statistics involved in (8). There is a compromise between the number of scales to be used in (8) and the duration of the epochs in which the statistics is computed. The lowest scales (high frequencies) should not include dominant noisy activity, whereas the largest scales (low frequencies) are limited by epoch duration and edge effects. Guidance on how to determine appropriate range of scales in our algorithm is provided in the GitHub (see also method 1.4). In summary, being intermediate between a fully time resolved continuous wavelet transform (not suitable for signal processing) and a Fourier analysis (not suitable for time resolved analysis), this tradeoff between accuracy of the scale-free model and the precision in time is precisely the benefit of the present approach based on the multi-scale representation of the signal.

1.3 The Wavelet – RnB: Estimation of the Rhythmic Signal*

Let us consider the wavelet expansion of a signal for with a wavelet basis accounting for the scale-free property of the signal as characterized with β^* as calculated in (8),

$$s(t) = \sum_j \sum_{k=1}^{n_j} w_{j,k}\;\; \psi_{j,k}^{(\alpha+\beta^*/2)}(t) \tag{9}$$

The wavelet coefficients $w_{j,k}$ (scale j, time k) are given by the scalar product (correlation) between the signal and the 'little wave', i.e. $w_{j,k} = \langle s,\ \psi_{j,k}^{(\alpha+\beta^*/2)} \rangle$ as illustrated in Fig.M1. In Equation (9), the summation over j ranges from 1 to J. This largest scale is chosen so that the frequency range of this multiresolution decomposition covers the entire frequency range of the rhythmic activities of interest (as illustrated in Fig.M1F where the sampling frequency is 200 Hz, the approximate correspondence between scales and frequencies is explained in the GitHub repository). The discrete wavelet coefficients displayed in Fig.M1C illustrate the stationary gaussian process that governs the wavelet coefficients at each scale, of a signal mostly driven by a scale-free process.

The 'fractional spline wavelet' bases have been chosen to handle the non-integer regularity quantified with the parameter $\alpha' = \alpha + \beta^*/2$' and defines a wavelet filter acting as a fractional differentiation,

$$\langle s, \psi_{j,k}^{(\alpha')} \rangle \ \approx\ 2^{j\,(\alpha'+3/2)}\ \partial^{\alpha'+1} s\big(k\,2^j\big) \tag{10}$$

where the partial differentiation operator ∂^r corresponds to a Fourier-domain product with f^r. The following equality can be further shown,

$$\langle \partial^{\frac{\beta^*}{2}} s, \psi_{j,k}^{(\alpha)} \rangle = \mathcal{K}\left(\alpha + \frac{\beta^*}{2}, \alpha\right)\ 2^{-j\,\beta^*/2}\ \langle s, \psi_{j,k}^{(\alpha+\beta^*/2)} \rangle \tag{11}$$

where

$$\mathcal{K}(\alpha', \alpha) = (4\pi)^{\alpha'-\alpha}\ \frac{2^{\alpha}-1}{2^{\alpha'}-1}\ \frac{\zeta(\alpha+1)}{\zeta(\alpha'+1)} \tag{12}$$

Relation (11) suggests that a whitening correction combined with a change of wavelet basis allows to synthetize a time-resolved fractional differentiation, able to remove the arrhythmicity from the original signal,

$$s_R(t) \stackrel{\text{def}}{=} \sum\nolimits_j \sum\nolimits_{k=1}^{n_j} \langle \partial^{\frac{\beta^*}{2}} s, \psi_{j,k}^{(\alpha)} \rangle\ \ \psi_{j,k}^{(\alpha)}(t) \tag{13}$$

Notice that the fractional differentiation $\partial^{\beta^*/2}$ of the original signal is precisely the whitening filtering of the power expressed by $Q(f)^{-1}\,\Gamma(f)$ in (2). Formula (13) expresses this 'spectral operation' in the time domain. To summarize, the 'rhythmic signal' is defined by

$$s_R(t) = \sum\nolimits_j \sum\nolimits_{k=1}^{n_j} w_{j,k}^*\ \ \psi_{j,k}^{(\alpha)}(t) \tag{14}$$

with

$$w_{j,k}^* = \mathcal{K}\left(\alpha + \frac{\beta^*}{2}, \alpha\right)\ 2^{-j\,\beta^*/2}\ \mathcal{S}\big(w_{j,k}\big)$$

computed from the wavelet analysis of the original signal (9). A denoising shrinkage $\mathcal{S}$ has been introduced to keep the significant largest wavelet coefficients. It is worth mentioning that each epoch will be analyzed with its appropriate wavelet basis parametrized with a specific β^* whereas the synthesis (14) is performed in a unique wavelet basis parametrized with α. In practice, the

regularity of the rhythmic signal is accomplished with $\alpha > 2$. The wavelet analysis of an original signal and the synthesis of a rhythmic signal is illustrated respectively on Fig.M1C and Fig.M1E.

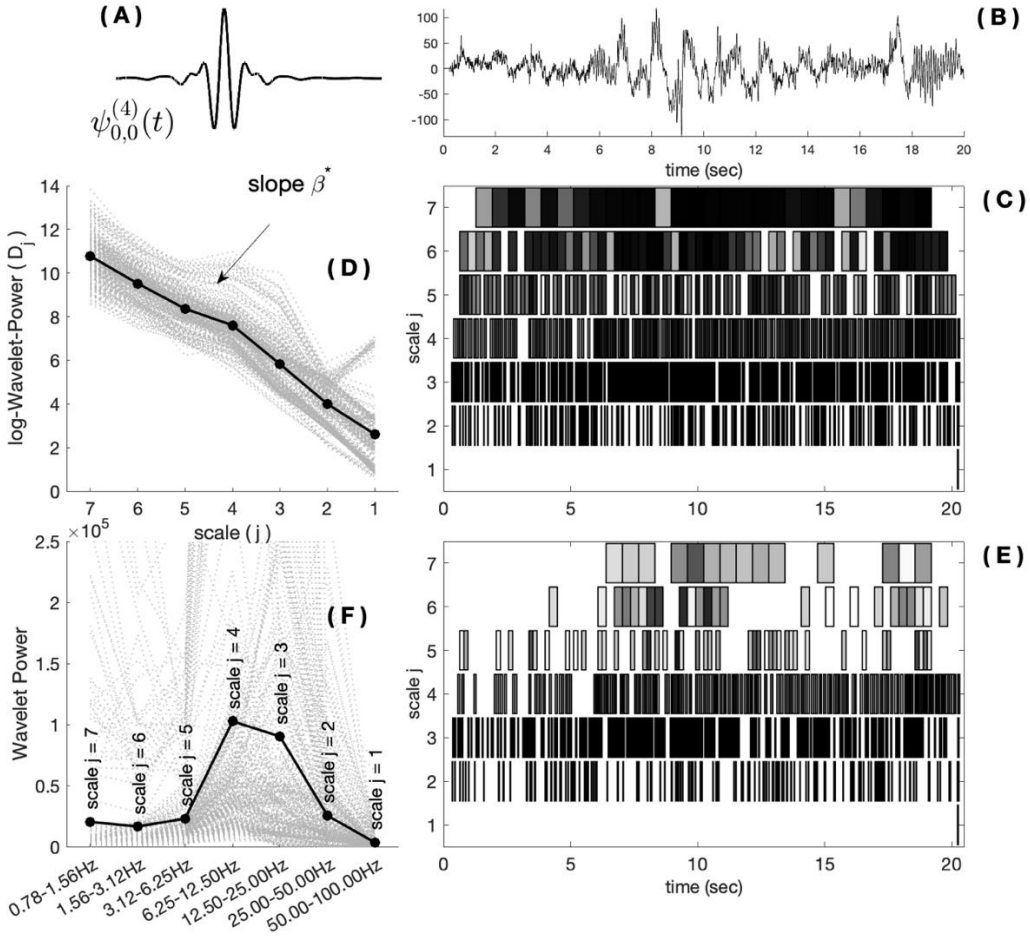

Fig.M1 **The analysis and synthesis of a signal using fractional spline wavelets.** (A) An example of fractional spline wavelet that could be used for analysis of an EEG signal as illustrated in (B). (C) 'time-scale' decomposition of $s(t)$ displayed in (B) using wavelet basis generated with (A). Each boxes represents a wavelet coefficient $\langle s, \psi_{j,k}^{(4)} \rangle$ at a particular scale (j) and discrete time ($k\ 2^j$). The real time is indicated on the x-axis. To help the reading of the time-scale representations, visible boxes account for 99% of the overall wavelet power of the signal. Gray intensity (globally normalized) indicates the amplitude of the largest wavelet coefficient. (D) Logarithmic wavelet power of (B) with respect to the dyadic scale parameter. The linear regression will provide the scaling exponent as given by (8). (E) 'Time-scale' decomposition of the rhythmic signal resulting from processing (B). Notice the lacunar representation as compared to the analysis of the original signal in M1C. The rhythmic decomposition exhibits coefficients at large scale (low frequencies) that seem to account for oscillatory pattern localized in time (confirmed with an inspection of (B)). (F) Wavelet power of multiple rhythmic signals (dashed grey lines) and the mean (dark bold line).

Although the arrhythmic characteristic of the original discrete wavelet coefficients is clearly attenuated in the discrete wavelet representation of the rhythmic time series (see Fig.M1E), the

wavelet power of the rhythmic signal does not exhibit the details of the oscillatory content since its representation is driven by time-scales (Fig.M1F). However, the Fourier power spectrum of the synthetized rhythmic signals will be appropriate to extract the oscillatory components. From a collection of physiologically equivalent epochs (NREM3 for instance), the average of the spectral power densities from the rhythmic signal provides an inventory of rhythms called here 'spectroscopy', as illustrated on figure Fig.M2C. In addition to this spectral signature, we have the distribution of the β-exponent that characterizes the arrhythmicity of the rhythm's background.

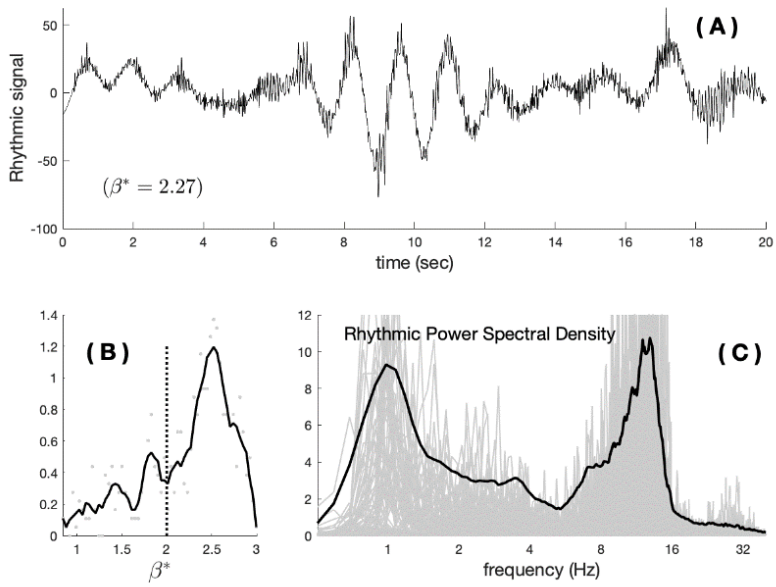

Fig.M2 **The 'Rhythmic spectroscopy'.** (A) The rhythmic signal corresponding to (B) and synthetized from (E) in Fig.M1. The value of the β-exponent of the removed arrhythmic component is indicated in parenthesis. (B) From 300 epochs (NREM3, Anterior Cingulate), the probability distribution of the β-exponents. (C) From 300 epochs (NREM3, Anterior Cingulate), the individual rhythmic spectrums and the 'rhythmic spectroscopy' provided with the mean (bold line).

1.4 Wavelet-RnB – the algorithm

In the following sections, the wavelet-RnB algorithm will be used on simulations and intracranial sleep recordings. Description on how to use this algorithm on user-provided data can be found in a publicly available GitHub (https://github.com/michaelcfoti/RnB-Wavelet/). Code for this algorithm is available as a Matlab package licensed by an Apache 2.0 license. The module supports Matlab2021a or later, with dependencies upon the 'Signal Processing' toolbox. The package is openly developed and maintained. The project's repository includes the codebase, a demo which allows to illustrate use of the algorithm on publicly available and user-provided data and the documentation materials. This pipeline allows to process user-provided timeseries, to extract a rhythmic timeserie and perform basic a spectroscopy. The rhythmic timeseries is extracted as a matrix that can be used by user to perform time-resolved analyses.

Two parameters need to be set to use the algorithm on user-provided data (see the *wRnBMain* script in the Github). The parameters linked to the beta estimation relate to the $j1$ and $j2$ scale range (methods 1.2) in the β' estimation. The parameter J refers to the highest scales (lower frequency) upon which the wavelet analysis/synthesis operations are performed to obtain the rhythmic signal, similarly to a high-pass filter. These parameters can be changed according to the input data properties and the documentation on the GitHub allows to understand the impact of such changes. Standard values are proposed as were used to perform the following analyses. As default parameters used in the following analyses, the scale run from 1 to 9 to determine the arrhythmic β's and the parameter J was set to 8.

*2.1 Simulations of scale-free time series and neural mass oscillation **

Simulations were performed to assess the performance of the Wavelet-RnB approach to characterize background and rhythms. Simulations considered a mixture of various scale-free backgrounds with transient oscillations, based on an elementary neural mass model. Considering a fractional Brownian motion (fBm) kind of signals, the backgrounds were obtained by filtering a white-noise time series in the frequency domain to obtain a power law $1/f^{\beta}$ of the spectral power while keeping the random Fourier phase. To simulate the variability of the background, for a batch of simulations trials, a β-exponent was randomly chosen around a value, and epochs were generated with a standard deviation of 0.1.

The neural mass time series was obtained from the classical phenomenological model proposed by Jansen and Ritt [53,54]. This dynamical model is based on coupled inhibitory and excitatory neuronal populations in interaction with a pyramidal cell. The canonical temporal and spectral responses of such a model is shown on Fig.M3. As described previously [53], the spectral response of a neural mass model corresponds to the filtering of an input white noise. For further simulations, the neural mass response was added to pure scale-free backgrounds (see 2.2 below).

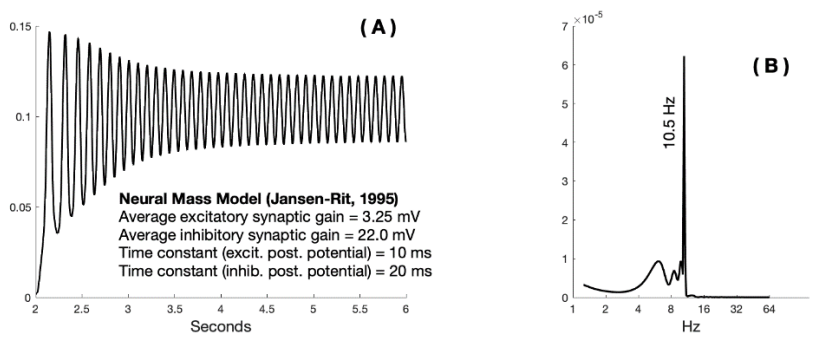

Fig.M3. **Neural mass oscillation**. (A) A four second oscillation produced by a standard neural mass model (with the original parameters). (B) The Fourier power spectrum of the response (A). The alpha peak is accompanied with a lower frequency content that corresponds to the first seconds of the oscillation that does not reach a 'pure' harmonic oscillation.

2.2 Simulations of rhythmic timeseries and validation of Wavelet-RnB

Following the model expressed in (5), 'realistic' simulations consisted in eight seconds epochs of pure 'scale-free' background, in which short duration lasting oscillations were added in a subset of samples. In a first series of simulation, 300 pure 'scale-free' epochs were generated with a scaling exponent randomly defined around a fixed value, i.e. 1.7 with a standard deviation of 0.1. Then, 200 randomly chosen time series were selected to incorporate a four second oscillation generated with the neural-mass oscillation (see Fig.M3A). 60 epochs were randomly generated for analyses as illustrated in Figure M4.

In this analysis, we investigated how the arrhythmic background impacts the wavelet-RnB estimation of the rhythmic amplitude. We simulated an alpha (10.5 Hz) oscillation with 15 amplitude levels, in three arrhythmic background conditions (1.7, 2.1 and 2.5). 60 simulations were performed per amplitude level and arrhythmic background conditions. Linear regressions were used to assess the relationship between simulation parameters and wavelet-RnB estimates of the maximal amplitude in each spectrum. Simulations parameters (oscillation amplitude and arrhythmic background) and their interactions were entered as predictors of RnB-wavelet outcomes.

Although the non-linearity of wavelet-RnB estimator, the rhythmic estimations (amplitude out) scaled remarkably linearly with the amplitude of the simulated oscillations (amplitude in) (*b*=0.99, p<0.0001, R^2=0.98). Rhythmic estimations differed slightly between the three arrhythmic conditions (interaction: t=8.58, p<0.0001; R^2<0.01), although they remained strongly associated with the amplitude of the simulated rhythm in each of the background conditions (*b*=0.99 to *b*=0.94 from lower to higher scale-free exponents, p<0.0001 in the three arrhythmic conditions).

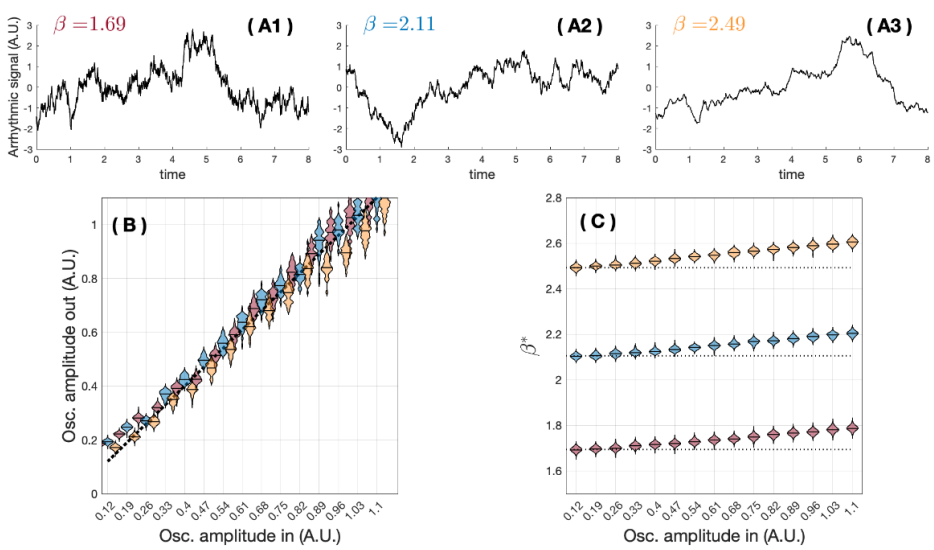

Fig.M4.

Wavelet' RnB estimation of rhythms and arrhythmic background. A1, A2, A3. Examples of simulated $1/f^{\beta}$ time series with three different values of arrhythmic background (β) (red: 1.69, blue: 2.11, yellow: 2.49); 300 simulations were generated for each arrhythmic condition. For a random set of 200 arrhythmic simulations, an alpha oscillation (10.5 Hz) was added, varying its amplitude at 15 fixed amplitude levels (x-axis on the B plot). For each amplitude level, RnB is applied 60 times on a

random selection among all epochs, enforcing a realistic approach where an oscillation may or may not be systematically present. **B.** Estimated maximal rhythmic amplitude measured by RnB (Y-axis) plotted against simulated alpha oscillation amplitudes (X axis). Colors of the dots represent the arrhythmic conditions (red: $\beta = 1.69$; blue: $\beta = 2.11$; yellow: $\beta = 2.49$). **C.** Distributions of the estimated scaling exponents out (Y axis) with respect to the simulated alpha oscillation amplitudes (X axis) for the three simulated arrhythmic backgrounds. The dashed line indicates the value in the simulation.

Second, we evaluated whether RnB estimates of the arrhythmic background (scaling exponent) were impacted by the amplitude of the simulated alpha oscillation (Fig.M4C). As expected, the three simulated arrhythmic background conditions were strongly associated with RnB estimates of the arrhythmic background (β; change in constant, t=663.3, p<0.0001, R^2=0.99). In addition, higher amplitude of the simulated alpha oscillation was associated with higher estimates of the arrhythmic background (β; change in slope; b=0.10, t=91.1, p<0.001, R^2<0.01), although this relationship differed slightly between the three background conditions (interaction; t=9.47, p<0.001; R^2<0.001; b=0.10 to b=0.11 across the three background conditions).

Another batch of simulations were conducted to assess the ability to address multiple rhythmic oscillations. With a similar strategy as for the neural mass simulations, we consider a random set of 300 scale-free timeseries (mean exponent = 2.5 and variance = 0.01) to which a combination of two oscillations (3 Hz and 13 Hz) were added in a 200 epochs subset (Fig.M5B and M5C). The simulation consisted of varying the amplitude of the 3 Hz oscillation only, keeping constant the amplitude of the 13 Hz oscillation. As previously, 60 samples were randomly selected from the pool of 300 epochs for analysis.

As expected, the rhythmic amplitude estimation for the delta oscillation (amplitude out) scaled linearly with the amplitude of the simulated oscillation (amplitude in; Fig.M5D, *b*=0.87, p<0.0001, R^2=0.85). There was no significant relationship between the amplitude of the simulation delta oscillation (amplitude in) and the estimated maximal sigma amplitude (Fig.M5E; *b*=-0.01, p=0.27, R^2 < 0.01). Wavelet-RnB slightly overestimate the calculated exponent in presence of multiple oscillations, but this does not scale with the amplitude of the simulated delta oscillation (Fig.M5F, constant=2.7, p<0.001, *b*=-0.03, p=0.31, R^2=0.001).

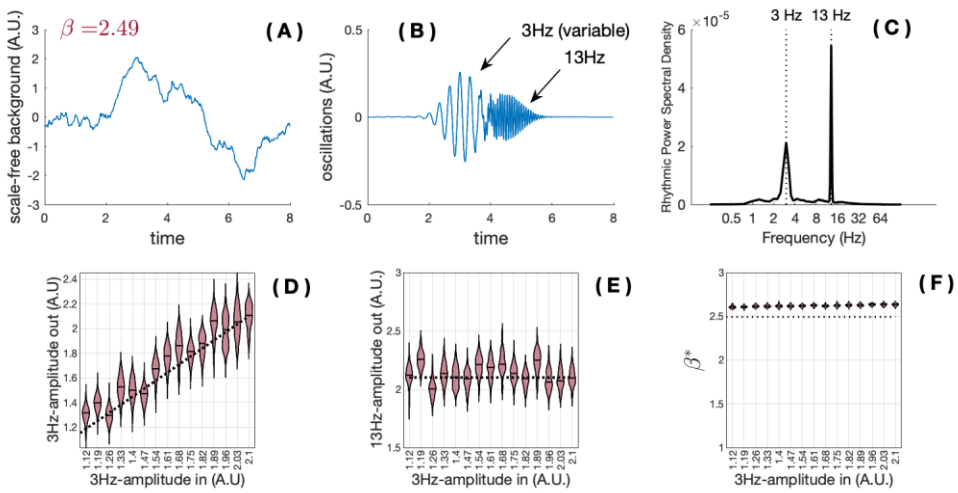

Fig.M5. **Wavelet-RnB and multiple oscillations**. (A) An example of scale-free time series. (B) An example of rhythmic oscillations to be added to (A). (C) Spectral signature of the rhythmic component (B). (D) Response of RnB regarding the amplitude of the 3 Hz-oscillation with respect to varying amplitude of this oscillatory component. (E) Response of the RnB regarding the constant amplitude 13 Hz-oscillation with a varying amplitude of the 3 Hz-oscillation. (F) Response of the RnB algorithm regarding the scale-free exponent in a varying amplitude of the 3Hz-oscillatory component.

3. Analyses of the intracranial sleep recordings

The intracranial recordings used in this work are extracted from the MNI-open iEEG atlas (https://mni-open-ieegatlas.research.mcgill.ca)[18]. From this multicentric database that provides us with an exhaustive exploration of the physiological activity of non-lesional tissues of the sleeping brain, we consider the recordings from all the electrodes localized in the precuneus and the anterior cingulate, during the NREM2 and NREM3 stages.

The characteristics of this selection are described in the following table.

Region	stage	# patients	sampling	# epochs	duration
Precuneus	NREM2	16 patients	200 Hz	967	322.33 min
	NREM3	16 patients	200 Hz	951	317 min
Ant. Cingulate	NREM2	16 patients	200 Hz	821	273.66 min
	NREM3	16 patients	200 Hz	809	269.66 min

The FOOOF algorithm has been applied on the averaged power spectrum of the intracranial data with the parameters listed below. The gaussian expansion of the 'periodic peaks' provided by this algorithm are shown in Fig.4 (B1, B2).

Region	stage	Frequency range	Peak width limits	# peaks	Aperiodic mode
Precuneus	NREM2	0-45 Hz	1-8 Hz	3 max.	fixed
	NREM3	1-45 Hz	1-8 Hz	3 max.	fixed
Ant. Cingulate	NREM2	0-45 Hz	1-8 Hz	3 max.	fixed
	NREM3	1-45 Hz	1-8 Hz	3 max.	fixed

*3.1 The Sleep Slow Waves (SSW) detection**

The SSW detection followed the usual approach for intracranial EEG[22]. First, zero-crossing markers are obtained in the filtered signal (with the appropriate delta band, e.g. 0.5-4Hz). Since the polarity of the intracranial recordings cannot be interpreted regarding the neurophysiological activity, the depolarization phase of the SSW was defined as the phase of the SSW with the higher gamma (> 32 Hz) power.

The original SSW inventory was obtained from the standard delta bandpass (0.5–4 Hz) filtering of the raw signals. Averaged detected SSW are shown on Fig.M6A1, and M6A2. They were co-registered around their hyperpolarization, in the two regions of interest. As expected, induced sigma activity was suppressed during the hyperpolarization phase in both regions (Fig.M6 B1 and C1 and Fig. M6 B2 and C2).

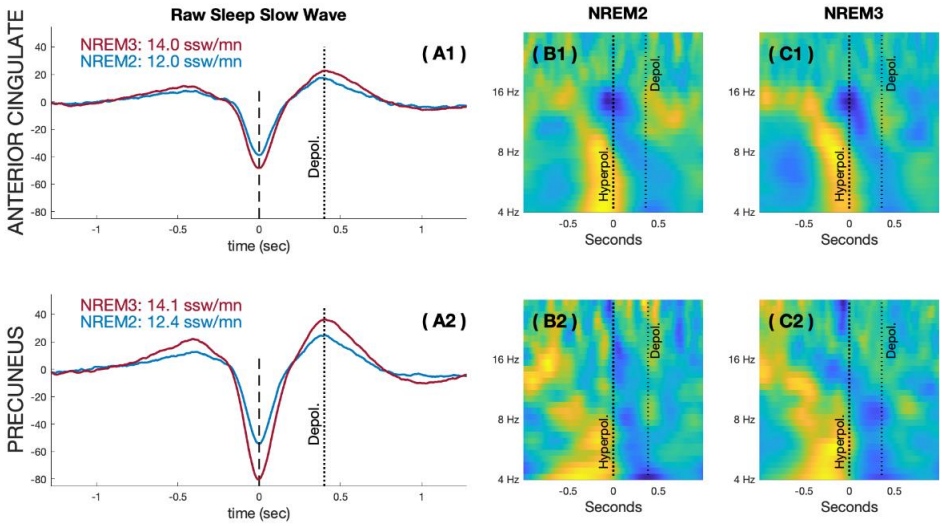

Fig.M6.
Slow waves detection and time-frequency characterization in the original timeseries. SSWs waveform in the anterior cingulate (A1) and precuneus (A2) are shown, alongside density (nb/min) during NREM2 and NREM3 sleep. The induced time frequency planes associated with slow waves are shown on the right, during NREM2 (B1, B2) and NREM3 (C1, C2).

The rhythmic SSW (rSSW) inventory consisted of using the previous algorithm on the rhythmic signal. Then, a second pass was performed in which the band-pass filter was adapted for the specific rhythmic mode found in the delta band spectroscopy of the region, and each sleep stage (Fig. 5).

The averaged rhythmic SSWs are displayed on Fig.M7(A1, A2). Spectrograms (see subsection 4.2) showed rhythmic sigma around the hyperpolarisation predominantly in the anterior cingulate and during NREM3 sleep (Fig.M7, C1 and C2).

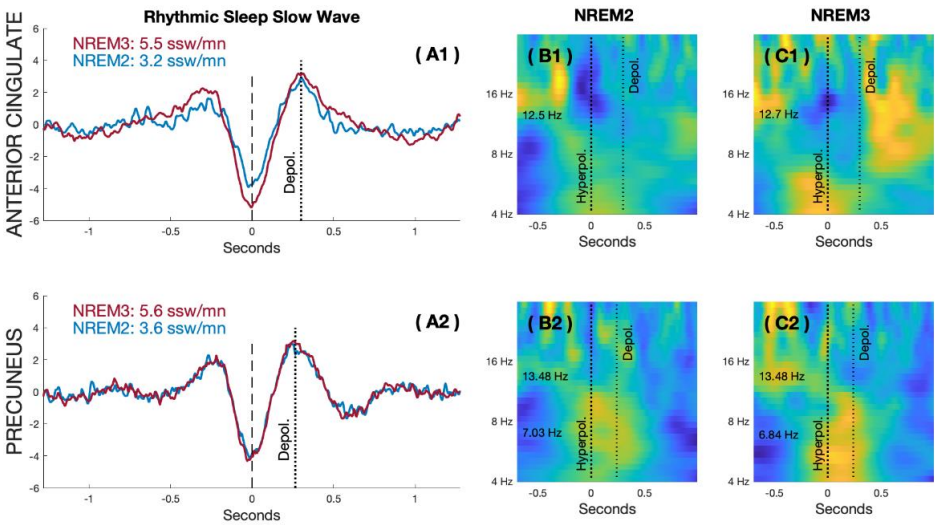

Fig.M7. Rhythmic slow waves detection and scalogram characterization (rhythmic time series). SSWs waveform in the anterior cingulate and precuneus are shown with density and count rate in NREM2 and NREM3 sleep. The induced time frequency planes are shown on the right, with NREM2 (B1, B2) and NREM3 (C1, C2).

*3.2 Slow and Fast Switchers**

It was previously shown that SSW can be clustered with respect to their transition frequency, that is defined in terms of the delay (τ) between the down phase (hyperpolarization) and the up phase (depolarization) of the slow wave[23]. SSWs are either 'slow' or 'fast' switchers, depending on the transition frequency. Here, we performed this categorization of slow waves using an unsupervised mixture of Gaussians (EM algorithm) able to estimate the latent 'switcher' class of each SSW. This categorization was obtained both in the original inventory of SSWs and in the rSSWs inventory.

*3.3 The Theta bursts (TB) detection**

Theta bursts (TBs) were detected by adapting a previously reported procedure[26] using our sleep spectroscopy. We adapted the theta-band filter according to the theta mode obtained from the rhythmic spectrum in the precuneus (6.84 ± 2.4 Hz in NREM2 and 7.02 ± 2.4 Hz in NREM3). The detected events had peaks above ± 3 standard deviation of the average power across the epochs with start and stop times defined with ± 1 standard deviation. The final TBs inventory kept events with a duration between 0.4 and 1 second. Figure M8 shows averaged TBs co-registered with respect to the maximum of the envelop of the Hilbert transform. As shown on Fig.M8(B1) and (B2), the scalogram of these averaged signals exhibited the sigma activity locked with the TB's.

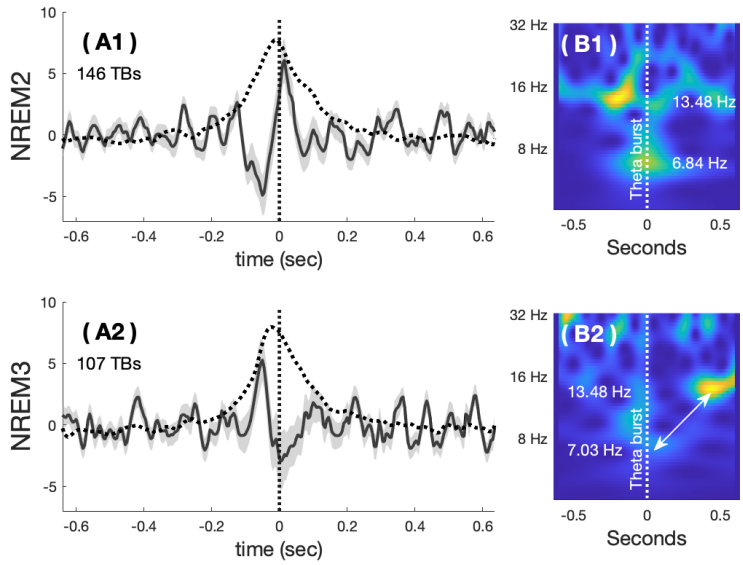

Fig.M8 **Time-frequency analysis of theta bursts coupled to SSWs during NREM sleep.** Average waveform of a theta burst is shown on the left (A1 and A2). In each plot, the dashed line is the average of the Hilbert envelops in the theta band. The TBs have been co-registered with respect to the maximum envelop of each event. The dashed line represents the average of the envelops. Phase-locked time-frequency analysis is shown on the right (B1 and B2; see wavelet and time-frequency analyses section). The TBs have been co-registered with respect to the maximum envelop of each event. The dashed line represents the average of the envelops. In (B2), the arrow emphasizes the synchronization with a sigma locked activity as also shown in Fig.8.

4.1 Spectroscopy analyses

We produced figures alike to M2B and M2C to investigate how rhythmic and arrhythmic activity was modulated by different NREM-specific factors. This is what we consider NREM sleep spectroscopy. We considered the effects of sleep stage, of the presence and absence of a slow-wave relative to a baseline, and between fast and slow switchers.

To formally test an effect of switcher type on the NREM spectroscopy, we used non-parametric Wilcoxon rank test for the arrhythmic estimations the β distributions were either highly skewed or bimodal (see Fig.6, main text). We used t-tests to investigate differences in rhythmic power averaged in frequency bands common to both switchers in each region (Fig. 6Anterior Cingulate: 0.5-4 Hz; 8-14 Hz; Precuneus: 0.5-4 Hz; 11.5-14.5 Hz).

*4.2 Wavelet and time-frequency analyses**

Scalograms were obtained with the continuous wavelet transform using the Morse analytic wavelet with default parameters ($\beta = 20$ and $\gamma = 3$). For visualization only, each time-frequency planes are renormalized using an analytic variant of the Taeger-Kaiser power normalization and each display is individually rescaled between 0 and 1[55].

Averaging the amplitude of the wavelet coefficients across the trials will highlight an induced power locked to the chosen landmark, whereas the amplitude of the average of wavelet coefficients will exhibit the synchronous time-frequency locked characteristics.

The time-frequency wavelet transform of each SSWs was calculated and averaged with respect to a common landmark (indicated by $t = 0$ in the figures), either the hyperpolarization phase (as in Fig.M6 and Fig. 6M7) or the half-transition (or zero-crossing, as illustrated in Fig.7).

*4.3 Phase-Amplitude Coupling analyses**

We computed a phase-amplitude coupling (PAC) estimate for each epoch with SSWs or rSSWs using the phase $\varphi(t)$ of the delta band (0.5-4hz) and the amplitude of the simultaneous sigma activity (10-16 Hz) in the original signal. For rSSWs, we considered the phase $\varphi(t)$ of the delta band (0.5-4 Hz) and the amplitude of the simultaneous sigma activity in the rhythmic timeseries (rPAC). For rPAC, we adapted the sigma frequency band as defined by the RnB spectroscopy in each region (Anterior Cingulate: 8-14 Hz; Precuneus: 11.5-14.5 Hz).

For each epoch, the PAC is defined by[56]

$$PAC = \left| \frac{1}{T} \sum_t A(t)\, e^{i\,\varphi(t)} - \frac{1}{T} \sum_t A(t)\ \frac{1}{T} \sum_t e^{i\,\varphi(t)} \right| \tag{15}$$

where T is the SSW duration across which the summation is running. The final PAC displayed and analyzed on Fig.8 was the averaged value across the SSWs in a particular region (Ant. Cingulate or precuneus), from the raw or rhythmic time series, for a particular stage (NREM2 and NREM3), a particular type (slow or fast switcher), and with or without a TB in the case of the precuneus. Mann-Whitney U-tests were used to test for PAC and rPAC differences in NREM2 and NREM3 separately.

Methods references

51. Dumeur, M., Wang, S. H., Palva, J. M. & Ciuciu, P. Multifractality in critical neural field dynamics. *arXiv* (2023) doi:10.48550/arxiv.2312.03219.

52. Abry, P., Wendt, H., Jaffard, S. & Didier, G. Multivariate scale-free temporal dynamics: From spectral (Fourier) to fractal (wavelet) analysis. *C. R. Phys.* **20**, 489–501 (2019).

53. David, O. & Friston, K. J. A neural mass model for MEG/EEG: coupling and neuronal dynamics. *NeuroImage* **20**, 1743–1755 (2003).

54. Jansen, B. H. & Rit, V. G. Electroencephalogram and visual evoked potential generation in a mathematical model of coupled cortical columns. *Biol. Cybern.* **73**, 357–366 (1995).

55. Boudraa, A.-O. & Salzenstein, F. Teager–Kaiser energy methods for signal and image analysis: A review. *Digit. Signal Process.* **78**, 338–375 (2018).

56. Penny, W. D., Duzel, E., Miller, K. J. & Ojemann, J. G. Testing for nested oscillation. *J. Neurosci. Methods* **174**, 50–61 (2008).

Data availability

All simulations performed as well as the code to replicate these epochs, have been deposited into a public repository (Github link). All sleep data reported and analyzed in this manuscript are secondary usages of data that was published in the MNI-open iEEG atlas.

Code availability

Matlab (R2021a) was used to code the analysis of the data. All the codes used in the analyses and for figure creation are openly available from the Github, which includes the code used for the simulations and NREM sleep analyses. The algorithm code is also available on GitHub, which allows the processing of user-imported data (https://...).

Extended figures and supplementary material

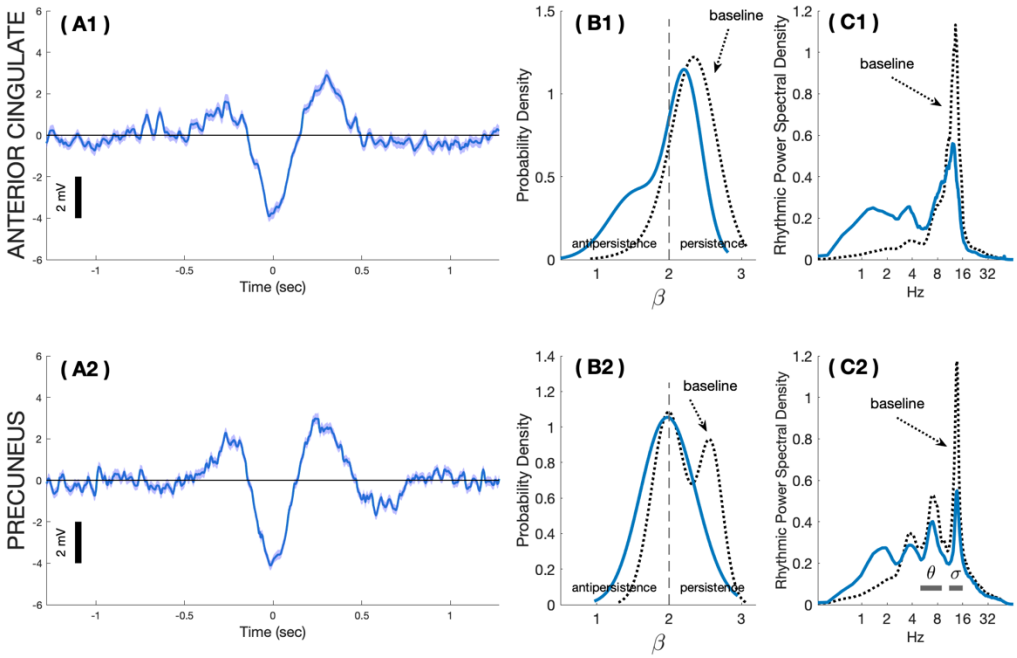

Extended Figure 5-1***.*** **NREM2,** Same legend as in Fig.5.

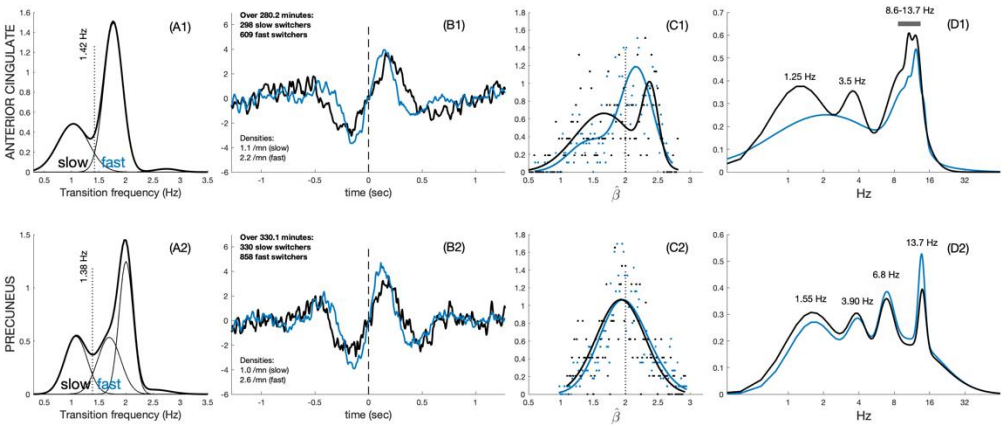

Extended Figure 6-1. **The spectroscopy of slow (rSlowS) and fast switchers (rFastS) during NREM3.** Same legend as in Fig. 6.

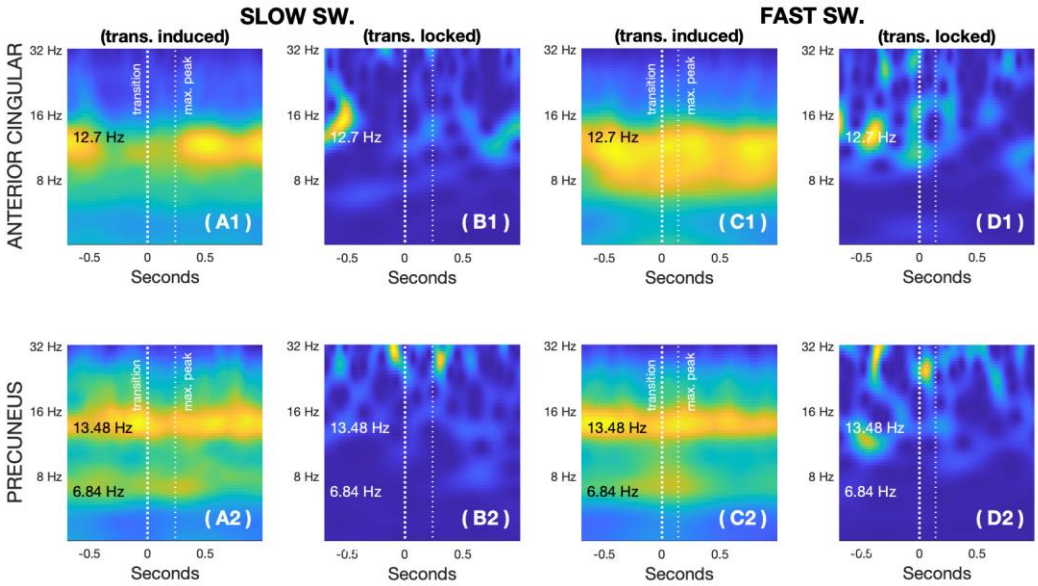

Extended Figure 7-1. **Induced and phase-locked rhythmic power synchronized with the transition of rSlowS and rFastS during NREM2 sleep**, Same legend as in Fig.7.

Supplementary table 1

Cerebral region	Sleep stage	Condition	PAC[1]	rPAC[1]	p-val[2]
Anterior cingulate	*NREM3*	Slow switchers	0.20 (0.11)	0.30 (0.16)	**<0.001**
		Fast switchers	0.21 (0.11)	0.27 (0.14)	**<0.001**
	NREM2	Slow switchers	0.20 (0.11)	0.29 (0.16)	**<0.001**
		Fast switchers	0.20 (0.11)	0.27 (0.13)	**<0.001**
Precuneus	*NREM3*	Slow switchers	0.19 (0.10)	0.25 (0.13)	**<0.001**
		Fast switchers	0.20 (0.11)	0.25 (0.12)	**<0.001**
	NREM2	Slow switchers	0.19 (0.10)	0.24 (0.13)	**<0.001**
		Fast switchers	0.20 (0.10)	0.25 (0.12)	**<0.001**

[1] Mean (standard deviation)
[2] p-value from U Mann-Whitney test (PAC vs rPAC)